Simulating complex tumor dynamics from avascular to vascular growth using a general level-set method

Cosmina S. Hogea[a], Bruce T. Murray[a], James A. Sethian[b]

[a]Department of Mechanical Engineering, Binghamton University, Binghamton, NY 13902, USA

[b]Department of Mathematics and Lawrence Berkeley National Laboratory, University of California, Berkeley, CA 94721, USA

* This author was supported in part by the Applied Mathematical Sciences subprogram of the Office of Energy Research, U.S. Department of Energy, under Contract Number DE-AC03-76SF00098, and the Division of Mathematical Sciences of the National Science Foundation

Abstract

A comprehensive continuum model of solid tumor evolution and development is investigated in detail numerically, both under the assumption of spherical symmetry and for arbitrary two-dimensional growth. To our knowledge, this is the first investigation of the multicell model developed by De Angelis and Preziosi (2000) as a moving boundary problem in higher dimensions and arbitrary geometries. The model represents both the avascular and the vascular phase of tumor evolution, and is able to simulate when the transition occurs; progressive formation of a necrotic core and a rim structure in the tumor during the avascular phase are also captured. In terms of transport processes, the interaction of the tumor with the surrounding tissue is realistically incorporated. A computational framework, based on a Cartesian mesh/narrow band level-set method, has been developed in order to solve the coupled advection-diffusion model equations with a moving boundary inside a fixed domain. The solution algorithm is designed so that extension to three-dimensional simulations is straightforward.

Keywords: *multicell model, avascular, vascular, tumor angiogenic factor, angiogenesis, vascularization, necrotic core, level set method, narrow band, finite differences*

1. Introduction

Over the last ten years, a number of important advancements have been made in the development of mathematical models to simulate the growth and macroscopic behavior of solid malignant tumors. The recent reviews by Araujo and McElwain [5] and Bellomo, et al. [6] contain extensive bibliographies and categorize the different solid tumor growth models. As in many areas of fundamental and applied science, the increasing sophistication of computational models make them an important part of the study of complex multi-scale phenomena. Verifiable computational models will likely become part of the arsenal of techniques used to better understand tumor evolution and treatment strategies in the near future. Continuum-based models can be used to help predict the evolution of a tumor's boundary in time and this knowledge may in turn help estimate the effect that various methods of treatment (e.g., chemotherapy, ultrasound) may have on the tumor behavior as well as on the surrounding healthy tissue and, ultimately, on the host.

Malignant solid tumors are masses of tissue formed as a result of abnormal and excessive proliferation of mutant (atypical) cells, whose division has escaped the mechanisms that control normal cellular proliferation. This abnormal proliferation of atypical cells can lead to uncontrolled growth, if not checked by the immune system. In simple terms, tumor growth (spread of malignant cells) can be described as follows: when fed with a sufficient amount of nutrient, malignant cells divide (cellular mitosis); when the density of cells in a specific volume becomes high, the cells are compressed by their neighbors and tend to move to less populated areas–where they may continue to proliferate–and this process is repeated. The growing tumor mass eventually begins to interact with the surrounding tissue and may eventually evolve in a complex manner.

There are different stages of a malignant tumor evolution; described roughly, the main stages are the cellular stage and the macroscopic stage. The cellular stage refers to the early stage of a tumor evolution, when proliferating tumor cells have not begun to agglomerate. The macroscopic stage comes about when clusters of atypical cells condense together into a compact shape (e.g., spherical); this stage is sub-divided into two subsequent phases–the avascular phase and the vascular phase. During the avascular phase, the tumor obtains nutrients via diffusion processes alone from the local environment. In the second phase, called the vascular phase, the tumor attempts to develop its own blood supply through the process of angiogenesis (i.e., the birth of new blood vessels). Malignant tumor cells secrete chemicals that diffuse outward into the surrounding healthy tissue and stimulate the growth of new capillary blood vessels; the newly formed blood vessels penetrate into the tumor mass feeding it with nutrients and leading to a rapid growth of the tumor (Folkman, [16]).

Due to the extremely complex nature of the biological systems underlying the behavior in tumors and to the limited understanding of tumor growth mechanisms, developing realistic models (mathematical, computational or both) is a difficult task. Currently, there are two major approaches for solid tumor growth modeling: the first employs continuum models to describe the evolution of the tumor in terms of systems of partial differential equations and/or non-linear integro-differential equations; the second approach uses discrete lattice or Cellular Automata (CA) models (e.g., Kansal, et al., [19]; Mansury and Diesboeck, [24]). For the macroscopic stage of tumor evolution, the continuum approach may offer the most generality. Assuming that all of the model parameters can be estimated, the advantage of a continuum model is that it provides a systematic means for evaluating the role played by individual physical mechanisms. However, the more complex the continuum model–the more difficult the computational simulations, since a continuum model will generally yield a nonlinear moving boundary problem described by systems of partial differential equations. The starting point for many continuum models is the pioneering work of Greenspan in the 1970's (see Araujo and McElwain, [5] and references therein). In recent years a variety of macroscopic continuum models have been derived employing analogies with inorganic systems (theory of mixtures, multiphase flow, e.g., Byrne, et al. [8] or Byrne and Preziosi [9]). While currently quite a few such complex models exist in the literature, computational simulations in arbitrary geometries and higher dimensions to further investigate and validate these models are still largely missing. Only very recently, such calculations have started to emerge [14],[40].

The goal of the present work is to investigate a recent comprehensive model DeAngelis and Preziosi (2000) [15], which involves multiple cell populations as well as chemical species. From a mathematical/computational point of view, the model is complex since it consists of a system of five PDEs, with some of the field variables as well as some of the coefficients discontinuous across the tumor boundary; the tumor surface evolves in time, and its location must be determined as part of the solution. At the same time, from a biological point of view, this model is very appealing for the following reasons: first of all, it captures both the avascular and the vascular stages of tumor growth (based on nutrient levels, the model predicts evolution from the avascular phase into the vascular one); second, it incorporates the interaction of the tumor with the surrounding environment (primarily in terms of the angiogenesis phenomenon); third, effects of potential treatments on the tumor evolution can be readily investigated by varying the model parameters.

A general computational framework for obtaining multi-dimensional solutions to continuum-based models for numerically simulating tumor growth has been developed and is described in Hogea, et al. [17]. In that work, the solution methodology is tested on a simplified, two-equation model. Finite-differences on a fixed Cartesian grid are employed to discretize the field equations, and the level set method is used to determine the location of the evolving tumor boundary. Here, the methodology is applied to the complex model involving coupled nonlinear reaction/advection/diffusion equations [15] in a two-region domain with an evolving tumor boundary.

The structure of the paper is as follows: Section 2 reviews the mathematical tumor growth model developed in DeAngelis and Preziosi [15]; Section 3 provides a brief description of the general formulation of the level set method; Section 4 investigates the spherically symmetric case –both from a biological and a computational point of view; a comparison of the tumor evolution in time simulated via two different numerical methods (a pseudo-Lagrangian and a level set – Eulerian one respectively) is performed; Section 5 presents the numerical algorithms for higher dimensions and arbitrary geometries; Section 6 contains two-dimensional simulations of tumor evolution in arbitrary geometries and various case scenarios for the model considered here; finally, Section 7 contains some remarks regarding further research.

2. Tumor growth model description

De Angelis and Preziosi [15] present a detailed derivation of the mathematical model under investigation here. The model is summarized below. A slightly modified version is reconsidered in Chaplain and Preziosi [11]. Geometrically, there are two regions in the model: *the inner region occupied by the tumor mass* is time-dependent and denoted by $\Omega(t)$; the tumor region is embedded in a larger fixed domain denoted by *D*. The region $\Omega^{out}(t) = D - \Omega(t)$ is referred to as *the (tumor) outer environment*.

There are two classes of **model dependent variables** characterizing the physical state of the biological system (i.e., in both the tumor mass and the outer environment): cell populations and chemical species (macro-molecules). They are essentially different: the cell size is much larger than that of the macro-molecules; the cells are delimited by a membrane and can not penetrate each other; they occupy actual physical space. By contrast, the chemical species consist of macro-molecules that may diffuse in the intercellular space, attach to the cell membrane or penetrate it, such that they actually do not take up physical space.

The following cell populations and chemical species are defined:

- **living tumor cells –** represented by the density $u_T = u_T(\vec{x}, t)$
- **dead tumor cells –** represented by the density $u_D = u_D(\vec{x}, t)$
- **new capillaries** (i.e., endothelial cells) with density $u_C = u_C(\vec{x}, t)$
- **nutrient concentration** $u_N = u_N(\vec{x}, t)$
- **tumor angiogenic factor (TAF) concentration** $u_A = u_A(\vec{x}, t)$

In a continuum mechanics framework, a standard mass balance law leads to a general reaction-advection-diffusion equation for each of the model variables introduced above:

$$\frac{\partial u}{\partial t} = \nabla \bullet (Q \nabla u) - \nabla \bullet (\vec{W} u) + \Gamma(u) - L(u) \tag{2.1}$$

where:

- $\Gamma = \Gamma(u)$ is the generation (proliferation/production) term;
- $L = L(u)$ is the death/decay term;
- $\vec{W}$ is the drift velocity field;
- Q is the diffusion coefficient.

The following modeling assumptions are made (from a biological viewpoint) in order to specify the exact form of Eq.(2.1) for each of the continuum model field variables:

I. Regarding the tumor cells (living and dead)

1. living tumor cells proliferate (cellular mitosis) only if the levels of nutrient reaching them are sufficient (i.e., above a certain threshold denoted by $\tilde{u}_N$);
2. living tumor cells die if the levels of nutrient reaching them are too low (i.e., below the threshold denoted by $\bar{u}_N$);
3. once a number of living cells inside the tumor have died due to insufficient nutrient, the nutrient becomes sufficient for the remaining ones to survive; thus, there is a smooth transition to a necrotic region;

4. when crowded by their neighbors, the living tumor cells have the ability to migrate towards lower density areas where they have higher chances of surviving and proliferating;
5. dead tumor cells do not move;
6. dead tumor cells are assumed to naturally disintegrate into waste products (water).

II. Regarding the tumor angiogenic factor (TAF)

1. living tumor cells are constantly producing TAF from a point on (in the revised version, the assumption is made that living tumor cells produce TAF only when they lack nutrient – i.e., haptotaxis occurs);
2. TAF diffuses both inside the tumor region and outside in the surrounding environment;
3. TAF naturally degrades

III. Regarding the new capillaries

1. endothelial cells reached by TAF are stimulated to proliferate (cellular mitosis) at a rate proportional to the concentration of TAF; proliferation decreases with the density of new capillaries; in particular, proliferation stops if the density of the new capillaries becomes higher than a certain threshold – here denoted by $\bar{u}_C$; the endothelial cells first stimulated are those belonging to the pre-existing capillary network, $\hat{u}_C = \hat{u}_C(\vec{x})$, in the tumor outer environment (the spatial distribution is prescribed initially in the model and is assumed time-independent);

2. new endothelial cells undergo both a random motion (diffusion) and an ordered one (chemotaxis) oriented towards the source of angiogenic stimulus (TAF) with formation of new capillary sprouts by accumulation of endothelial cells;
3. newly formed endothelial cells undergo apoptosis.

IV. Regarding the nutrient:

1. the nutrient in the tumor outer environment is provided by the capillary network at a linear rate; in particular, in the absence of new capillaries, the amount of nutrient in the tumor outer environment is constant;
2. diffusion of nutrient inside the tumor is promoted by the presence of capillaries, with the diffusion coefficient assumed to increase linearly with the density of capillaries;
3. nutrient is consumed by the living tumor cells.

The model assumes that all cells (living cells, dead cells and endothelial cells) equally contribute the *overall cell density* defined as:

$$u = u_T + u_D + u_C + \hat{u}_C \tag{2.2}$$

It is assumed that there is a threshold overall cell density – here denoted by $\bar{u}$ and called the *close packing density* (by analogy with multiphase flow terminology) – characterizing the fact that no pressure is felt by a cell when the total density u is equal to it (i.e. the stress vanishes for $u = \bar{u}$).

All the above modeling assumptions are placed in the context of the general advection-diffusion equation (2.1) for each of the field variables (densities or concentrations). For simplicity, assume that the diffusion coefficients for TAF and new capillaries are constant in D (in particular, this implies that they are continuous across the tumor boundary). The drift coefficients for the living tumor cells and endothelial cells are also assumed constant and positive. Under these last additional assumptions, the following **model governing equations** are employed here:

$$\text{- in } D: \quad \begin{cases} \dfrac{\partial u_A}{\partial t} = k_A \nabla^2 u_A + \gamma_A u_T - \delta_A u_A \\ \dfrac{\partial u_C}{\partial t} = k_C \nabla^2 u_C - w_C \nabla \bullet (u_C \nabla u_A) + \gamma_C u_A (\bar{u}_C - u_C)_+ (u_C + \hat{u}_C) - \delta_C u_C \end{cases} \tag{2.3}$$

and

$$\text{- in } \Omega(t): \begin{cases} \dfrac{\partial u_T}{\partial t} = w_T \nabla \bullet (u_T \nabla u) + \dfrac{\gamma_T u_N u_T}{\varepsilon} H(u_N - \tilde{u}_N u_T) - \delta_T H(\bar{u}_N u_T - u_N) u_T \\ \dfrac{\partial u_D}{\partial t} = \delta_T H(\bar{u}_N u_T - u_N) u_T - \delta_D u_D \\ \dfrac{\partial u_N}{\partial t} = \nabla \bullet [(k_E + k_N (u_C + \hat{u}_C)) \nabla u_N] - \delta_N u_T u_N \end{cases} \tag{2.4}$$

In the above equations it is naturally assumed that $u_T(\vec{x},t) = 0$ and $u_D(\vec{x},t) = 0$ if $\vec{x} \in \Omega^{out}(t)$ (in particular, they are discontinuous quantities across the tumor boundary), H is the Heaviside function: $H(u) = \begin{cases} 1\ , & if\ u > 0 \\ 0, & otherwise \end{cases}$ and $f_+ = \max(f, 0)$ denotes the positive part of the function f.

Production (growth) coefficients are denoted by γ; death (degradation) coefficients by δ; diffusion coefficients by k; transport (drift) coefficients by w. In the equation for the nutrient diffusion inside the tumor (last equation (2.4)), k_E stands for the diffusion coefficient in the absence of capillaries, while k_N measures the dependence of the diffusion rate on the presence of capillaries; both of them will be assumed constant here. In the evolution equation for the tumor living cells (first equation in 2.4), the parameter ε represents the amount of nutrient existent in the environment in the avascular phase. The function $\hat{u}_C = \hat{u}_C(\vec{x})$ (representing the density of the pre-existing capillaries) is modeled as a smooth function with compact support outside the domain occupied initially by the tumor. While various mathematical possibilities might exist to construct such a function to specifications - depending on the biological and/or computational instances, here the simplest case of a "bump function" shall be employed:

$$\hat{u}_C(\vec{x}) = \begin{cases} cons\tan t > 0, if\ \vec{x} \in S \subset \Omega^{out}(t=0) \\ 0 \qquad\qquad\quad , if\ \vec{x} \in D - O \end{cases} \tag{2.5}$$

where S represents the fixed region in space occupied by the pre-existing capillary network , with compact closure $\overline{S}$ and O is an open set arbitrarily close to S that contains $\overline{S}$.

Assuming that the tumor boundary is stress-free, that the nutrient at the tumor surface is the nutrient existent in the outer environment and that there are no dead cells at the tumor surface in the case of an expanding tumor, the following **boundary conditions** for the model governing equations (2.4) are imposed:

$$\text{- on } \partial\Omega(t): \begin{cases} u_T = \overline{u} - u_D - u_C - \hat{u}_C \\ u_N = \varepsilon + \beta(u_C + \hat{u}_C) \\ u_D = 0 \end{cases} \tag{2.6}$$

Also, assuming that the TAF and the new capillaries density tend to decrease substantially towards the boundaries of the tumor outer environment, the boundary conditions for the model governing equations (2.3) can be taken as:

- on ∂D: $$u_A = u_C = 0 \tag{2.7}$$

Treating the tumor boundary $\partial\Omega(t)$ as a material interface moving with the tumor cells at the tumor surface, its **normal velocity** is given by:

$$v = -w_T \nabla u\Big|_{\partial\Omega(t)} \bullet \vec{n}_{\partial\Omega(t)} \tag{2.8}$$

where $\vec{n}_{\partial\Omega(t)}$ is the local outward unit normal to the tumor boundary $\partial\Omega(t)$.

Finally, to complete the mathematical model, **initial conditions** are needed for the model governing equations (2.3) and (2.4):

- in D: $$u_A\big|_{t=0} = u_C\big|_{t=0} = 0 \tag{2.9}$$

- in $\Omega(t)\big|_{t=0}$: $$\begin{cases} u_T\big|_{t=0} = \bar{u} \\ u_D\big|_{t=0} = 0 \\ u_N\big|_{t=0} = \varepsilon \end{cases} \tag{2.10}$$

These initial conditions correspond to a realistic scenario at some point during the tumor avascular phase, where a nucleus consisting solely of uncompressed living malignant cells finds itself in an environment full of nutrient and starts releasing TAF to induce the angiogenesis process.

Using the same characteristic scale values as De Angelis and Preziosi [15], the following dimensionless variables are introduced:

$t^* = \gamma_T t$ (dimensionless time)

$\vec{x}^* = \sqrt{\dfrac{\delta_N \bar{u}}{k_E}}\vec{x}$ (dimensionless space)

$$U_j = \frac{u_j}{\overline{u}}\ ,\ j = T, D, C \tag{2.11}$$

$$U_N = \frac{u_N}{\varepsilon}$$

$$U_A = \frac{\gamma_T}{\gamma_A \overline{u}} u_A$$

By scaling the dimensional equations and boundary/initial conditions, the following two non-dimensional, coupled initial/boundary value problems are obtained [15]:

- in D^* **:**

$$\begin{cases} \dfrac{\partial U_A}{\partial t^*} = K_A \nabla^2 U_A + U_T - \Delta_A U_A \\ \dfrac{\partial U_C}{\partial t^*} = K_C \nabla^2 U_C - W_C \nabla \bullet (U_C \nabla U_A) + \Gamma_C U_A (\overline{U}_C - U_C)_+ (U_C + \hat{U}_C) - \Delta_C U_C \end{cases} \tag{2.12}$$

- on ∂D^* **:** $\quad U_A = U_C = 0$ (2.13)

- in D^* **:** $\quad U_A\big|_{t^*=0} = U_C\big|_{t^*=0} = 0$ (2.14)

- in $\Omega^*(t^*)$ **:**

$$\begin{cases} \dfrac{\partial U_T}{\partial t^*} = W_T \nabla \bullet (U_T \nabla U) + U_T U_N H(U_N - \tilde{U}_N U_T) - \Delta_T H(\overline{U}_N U_T - U_N) U_T \\ \dfrac{\partial U_D}{\partial t^*} = \Delta_T H(\overline{U}_N U_T - U_N) U_T - \Delta_D U_D \\ \dfrac{\partial U_N}{\partial t^*} = \Delta_N \{\nabla \bullet [(1 + K_N (U_C + \hat{U}_C)) \nabla U_N] - U_T U_N\} \end{cases} \tag{2.15}$$

- on $\partial\Omega^*(t^*)$ **:**
$$\begin{cases} U_T = 1 - U_D - U_C - \hat{U}_C \\ U_N = 1 + \mathrm{B}(U_C + \hat{U}_C) \\ U_D = 0 \end{cases} \tag{2.16}$$

- in $\Omega^*(t^*)\big|_{t^*=0}$ **:**
$$\begin{cases} U_T\big|_{t^*=0} = 1 \\ U_D\big|_{t^*=0} = 0 \\ U_N\big|_{t^*=0} = 1 \end{cases} \tag{2.17}$$

The corresponding scaled normal velocity of the tumor boundary is given by:

$$V = -W_T \nabla U\big|_{\partial\Omega^*} \bullet \vec{n}_{\partial\Omega^*} \tag{2.18}$$

In the scaled equations (2.12)-(2.18), spatial differentiation is with respect to the dimensionless spatial coordinate variables, represented in vector form by $\vec{x}^*$, and the following dimensionless model parameters (i.e., diffusion coefficients, drift velocities, growth/death coefficients and threshold densities) appear:

$$\begin{cases} K_A = \dfrac{k_A \delta_N \bar{u}}{k_E \gamma_T}, K_C = \dfrac{k_C \delta_N \bar{u}}{k_E \gamma_T},\ K_N = \dfrac{k_N \bar{u}}{k_E} \\ W_C = \dfrac{w_C \delta_N \gamma_A \bar{u}^2}{k_E \gamma_T^2}, W_T = \dfrac{w_T \delta_N \bar{u}^2}{k_E \gamma_T} \\ \Gamma_C = \dfrac{\gamma_C \gamma_A \bar{u}^2}{\gamma_T^2} \\ \Delta_N = \dfrac{\delta_N \bar{u}}{\gamma_T},\ \Delta_i = \dfrac{\delta_i}{\gamma_T},\ i = A, C, D, T \\ \tilde{U}_N = \dfrac{\bar{u}\tilde{u}_N}{\varepsilon},\ \bar{U}_N = \dfrac{\bar{u}\bar{u}_N}{\varepsilon},\ \bar{U}_C = \dfrac{\bar{u}_C}{\bar{u}},\ \hat{U}_C = \dfrac{\hat{u}_C}{\bar{u}} \\ \mathrm{B} = \dfrac{\beta \bar{u}}{\varepsilon} \end{cases} \tag{2.19}$$

In order to investigate the model behavior, Eqns. (2.12) and (2.15) with the prescribed boundary and initial conditions (2.13)-(2.14) and (2.16)-(2.17), respectively, are solved numerically to determine the unknowns U_A, U_C, U_T, U_D, U_N; the new location of the tumor boundary is then found by employing the normal velocity expression given by (2.18). In everything that follows, the "star" notation in all the above dimensionless model equations (2.12)-(2.18) is dropped for simplicity, and all references to the various model parameters (e.g., diffusion coefficients, drift velocities, etc) will be to the corresponding dimensionless parameters (2.19).

3. Level set formulation

As previously defined, let $\Omega = \Omega(t)$ denote the (scaled) domain occupied by the tumor, $\Omega^{out} = \Omega^{out}(t)$ the (scaled) tumor outer environment, and $\Sigma = \Sigma(t) = \partial\Omega(t)$ (a curve in 2D and a surface in 3D, respectively) be the boundary of the tumor, separating the tumor and the outside tissue. This boundary evolves in time with a normal velocity V given by Eq. (2.18), and the problem is finding the location of the tumor boundary at later moments in time starting from a known location at the initial moment of time $\Sigma_0 = \Sigma(t = 0)$. One way to do so is by employing the level set method introduced by Osher and Sethian [27] and based in part on the theory and numerics of curve evolution developed by Sethian [32],[33]. The basic idea behind the level set method is to introduce an additional variable, denoted by

$$\varphi = \varphi(\vec{x}, t),\ \vec{x} \in \Omega \cup \Sigma \cup \Omega^{out},\ t \in [0, \infty),$$

responsible for capturing the front $\Sigma = \Sigma(t)$ in an implicit fashion at each moment in time:

$$\Sigma = \Sigma(t) = \left\{ \vec{x} \,\middle|\, \varphi(\vec{x}, t) = 0 \right\}$$

The function $\varphi = \varphi(\vec{x}, t)$ is the level set function. First, the initial level set function value is set equal to the signed Euclidean distance function to the tumor boundary at the initial moment of time (taken negative inside the tumor and positive outside):

$$\varphi(\vec{x},0) = \begin{cases} -\,dist(\vec{x}, \Sigma_0)\ ,\ \vec{x} \in \Omega(t = 0) \\ 0, \quad \vec{x} \in \Sigma_0 \\ dist(\vec{x}, \Sigma_0)\ ,\ \vec{x} \in \Omega^{out}(t = 0) \end{cases} \tag{3.1}$$

At any moment in time, the location of the tumor boundary is given by the zero level set of the level set function. For a particle on the front with the path $\vec{x} = \vec{x}(t)$ one has:

$$\varphi(\vec{x}(t), t) = 0$$

The kinematics governing the motion of the boundary yields:

$$\frac{d\varphi}{dt} = \frac{\partial \varphi}{\partial t} + \nabla \varphi(\vec{x}(t),t) \bullet \frac{d\vec{x}}{dt}(t) = 0 \ , \ \forall t > 0$$

The outward unit normal on the boundary is given in terms of the level set function by:

$$\vec{n} = \frac{\nabla \varphi}{|\nabla \varphi|} \tag{3.2}$$

Substituting (3.2) in the above equation leads to the evolution equation for the level set function (initial value formulation):

$$\frac{\partial \varphi}{\partial t} + F|\nabla \varphi| = 0 \tag{3.3}$$

where $F = F(\vec{x},t), \ \vec{x} \in \Omega \cup \Sigma \cup \Omega^{out}, \ t > 0$ represents what is typically called an "extension velocity" field (i.e., defined everywhere, such that it always matches the given expression of the normal velocity V on the tumor boundary Σ):

$$F(\vec{x},t)\Big|_{\vec{x}\in\Sigma(t)} = V(\vec{x},t)\Big|_{\vec{x}\in\Sigma(t)} \tag{3.4}$$

Eq. (3.3) correctly moves the boundary with the prescribed normal velocity given by (2.18).

As compared to an explicit front-tracking formulation, there are considerable advantages of the level set formulation for this problem:

- the domain occupied by the tumor at each moment of time and the corresponding outer environment are apparent from the sign of the level set function (here taken negative the tumor region and positive outside);
- the local geometric properties of the tumor boundary (e.g. the normal) are readily available;
- the same formulation holds regardless of the number of spatial dimensions (1,2 or 3);

- enhanced implementations such as “the narrow band method” introduced by Adalsteinsson and Sethian [1] or “the fast marching method” [2],[34] are available that make the boundary capturing more computationally efficient.

On the other hand, some challenges arise when implementing the level set method:

- construction of the “extension velocity” field F in the level set equation (3.3) (generally, there is no natural choice for this field which is only defined on the interface itself);
- re-initialization of the level set function φ as a signed distance to the interface.

4. The spherically symmetric case

Solution procedures to the model equations (2.12) and (2.15) with the corresponding initial and boundary conditions are developed in this section under the assumption of spherical symmetry; both for computational purposes – to test the applicability of a level set approach – and for biological ones – to check the model behavior. The tumor is regarded as a growing sphere, of radius $R(t)$, with a given initial radius R_0. The model dependent variables $U_A = U_A(r,t), U_C = U_C(r,t), U_T = U_T(r,t), U_D = U_D(r,t)$ and $U_N = U_N(r,t)$, where r denotes the radial coordinate. The domain occupied by the tumor is then $\Omega = \Omega(t) = \{r \mid 0 \le r \le R(t)\}$, embedded into a larger fixed sphere of given radius R_D: $D = \{r \mid 0 \le r \le R_D\}$.

Each of the governing equations (2.12) and (2.15) can be cast in the general compact form:

$$\frac{\partial \mu}{\partial t} = \nabla \bullet (Q \nabla \mu) - W \nabla \bullet (\mu \nabla \nu) + \Gamma(\mu) - L(\mu) \tag{4.1}$$

where Q is constant and positive in Eqns. (2.12), zero in the first two Eqns. (2.15) variable in the last equation (2.15); W is constant and positive in the second equation (2.12), constant and negative in the first equation (2.15) and zero in all the remaining equations; ν depends explicitly on μ only in the first equation (2.15). In (4.1), μ and ν represent the various model dependent variables to be determined numerically. Rewriting (4.1) in spherical coordinates under the assumption of spherical symmetry ($\mu = \mu(r,t)$, $\nu = \nu(r,t)$, $Q = Q(r,t)$) yields:

$$\frac{\partial \mu}{\partial t} = \frac{1}{r^2}\frac{\partial}{\partial r}(r^2 Q \frac{\partial \mu}{\partial r}) - W \frac{1}{r^2}\frac{\partial}{\partial r}(r^2 \mu \frac{\partial \nu}{\partial r}) + \Gamma(\mu) - L(\mu) \tag{4.2}$$

For discretization purposes, it is convenient to rewrite (4.2) in non-conservative form:

$$\frac{\partial \mu}{\partial t} = Q\frac{\partial^2 \mu}{\partial r^2} + \frac{\partial Q}{\partial r}\frac{\partial \mu}{\partial r} + \frac{2}{r} Q \frac{\partial \mu}{\partial r} - W(\mu \frac{\partial^2 \nu}{\partial r^2} + \frac{\partial \mu}{\partial r}\frac{\partial \nu}{\partial r} + \frac{2}{r}\mu\frac{\partial \nu}{\partial r}) + \Gamma(\mu) - L(\mu) \tag{4.3}$$

The form (4.3) is preferred here mainly for two reasons: the contribution of lower order terms is individually highlighted for each of the model dependent variables – which makes a heuristic stability assessment [30] easy to conduct when a fully-explicit finite difference scheme is employed to solve numerically the nonlinear equations (4.3); then, in an Eulerian formulation, with a fixed grid and a moving boundary captured implicitly via a level set method, the spatial finite difference scheme at grid points adjacent to the boundary must be modified to take into account the prescribed boundary conditions. The latter is accomplished here by separately constructing second order interpolating polynomials for each of the model dependent variables – or, in the framework of Eq. (4.1), for each of the unknowns μ and ν. It is clearly then why a non-conservative version of (4.1), that will highlight the first order derivatives of μ and ν separately, is employed. However, an alternate ghost fluid method (GFM) formulation [26] allows for a conservative form.

Another aspect of primary importance when proceeding to the spatial discretization of the model Eqns. (2.12) – that are valid in the entire fixed computational domain D - is deciding whether to discretize them separately inside the region occupied by the tumor and outside respectively. This is the approach employed here, for the following reasons: in more general cases, the diffusion coefficients of TAF and of the new capillaries might be different inside the tumor and in the outer environment respectively; then, the production (source) term in the TAF equation is discontinuous across the tumor boundary; and finally, splitting the larger problem into two smaller ones – a domain-decomposition approach – is certainly very valuable in the perspective of a semi-implicit/implicit time discretization.

All the numerical results presented in this paper are obtained by employing a fully explicit (forward Euler) time discretization; alternate time-splitting/linearization schemes are currently under investigation by the authors – but the nonlinear diffusion type term $\nabla \bullet (U_T \nabla (U_T + U_D + U_C + \hat{U}_C))$ in the equation for the living tumor cells (the first equation (2.15)) coupled with the need to modify the spatial stencil at fixed grid points adjacent to a moving boundary make the problem challenging and computationally intensive; moreover, assessing the overall correctness and consistency [30],[38] of such schemes is a delicate aspect, particularly when no other results exist for comparison.

While the fully explicit method in an Eulerian framework with a moving boundary certainly leads to severe constraints on the time step, it naturally handles the fully nonlinear problem and the overall computational efficiency might prove equivalent to that involved in a less constrictive time-splitting method; the numerical results presented here shall show that a fully explicit method can be used as a basic computational tool to investigate the model behavior for model parameters in a certain range, particularly when no previous simulations have been performed and at least a preliminary assessment of the model from a biological point of view is desired.

4.1 A pseudo-Lagrangian solution method

For the spherically symmetric case it is possible to employ a coordinate transform and fix the location of the tumor boundary in the transformed domain (Landau transformation). A solution procedure using this method was developed for comparison purposes with the level set approach. For the tumor boundary location defined by *R(t)*, the following transformed coordinates are defined:

$$\begin{aligned} &\xi = \frac{r}{R(t)}\ ,\ 0 \le \xi \le 1 \\ &\eta = 1 + \frac{r - R(t)}{R_D - R(t)}\ ,\ 1 \le \eta \le 2 \end{aligned} \tag{4.4}$$

At each moment of time t, the inside of the tumor is being mapped onto the interval $[0,1]$, the outside of the tumor is being mapped onto the interval $[1,2]$ and the tumor boundary is located at $\xi = \eta = 1$. Employing the chain rule in (4.3) yields:

$$\begin{aligned}\frac{\partial \mu}{\partial t} = \xi \frac{\dot{R}(t)}{R(t)} \frac{\partial \mu}{\partial \xi} + \frac{1}{R^2(t)} [Q \frac{\partial^2 \mu}{\partial \xi^2} + \frac{\partial Q}{\partial \xi} \frac{\partial \mu}{\partial \xi} + \frac{2}{\xi} Q \frac{\partial \mu}{\partial \xi} - W(\mu \frac{\partial^2 \nu}{\partial \xi^2} + \frac{\partial \mu}{\partial \xi} \frac{\partial \nu}{\partial \xi} + \frac{2}{\xi} \mu \frac{\partial \nu}{\partial \xi})] \\ + \Gamma(\mu) - L(\mu), 0 < \xi < 1\end{aligned} \tag{4.5}$$

and

$$\begin{aligned}\frac{\partial \mu}{\partial t} = -(\eta - 2) \frac{\dot{R}(t)}{R_D - R(t)} \frac{\partial \mu}{\partial \eta} + \frac{1}{(R_D - R(t))^2} [Q \frac{\partial^2 \mu}{\partial \eta^2} + \frac{\partial Q}{\partial \eta} \frac{\partial \mu}{\partial \mu} - W(\mu \frac{\partial^2 \nu}{\partial \mu^2} + \frac{\partial \mu}{\partial \eta} \frac{\partial \nu}{\partial \eta})] \\ + \frac{2}{R(t) + (\eta - 1)(R_D - R(t))} \frac{1}{R_D - R(t)} (Q \frac{\partial \mu}{\partial \eta} - W \mu \frac{\partial \nu}{\partial \eta}) + \Gamma(\mu) - L(\mu), 1 < \eta < 2\end{aligned} \tag{4.6}$$

where $\dot{R}(t) = \frac{dR}{dt}(t)$.

Clearly, the model governing equations (2.15) satisfied inside the domain occupied by the tumor only are of the form (4.5), while the model equations (2.12) – valid in the entire computational domain – are split into two: inside the domain occupied by the tumor and outside respectively, thus they are of the form (4.5) - inside and (4.6) – outside. In this case, additional matching conditions at the tumor boundary are needed for the corresponding model dependent variables U_A and U_C respectively; these will be obtained by naturally assuming continuity of u_A and u_C and of the related fluxes

$(k_A \nabla u_A) \bullet \vec{n}$ and $(k_C \nabla u_C - w_C u_C \nabla u_A) \bullet \vec{n}$ across the tumor boundary, which here leads to:

$$\begin{cases} U_A\big|_{\xi=1} = U_A\big|_{\eta=1},\ U_C\big|_{\xi=1} = U_C\big|_{\eta=1} \\ \dfrac{1}{R(t)} \dfrac{\partial U_A}{\partial \xi}\Big|_{\xi=1} = \dfrac{1}{R_D - R(t)} \dfrac{\partial U_A}{\partial \eta}\Big|_{\eta=1} \\ \dfrac{1}{R(t)} \dfrac{\partial U_C}{\partial \xi}\Big|_{\xi=1} = \dfrac{1}{R_D - R(t)} \dfrac{\partial U_C}{\partial \eta}\Big|_{\eta=1} \end{cases} \tag{4.7}$$

Symmetry boundary conditions are employed at the tumor center $r = 0$:

$$\frac{\partial U_A}{\partial \xi}\Big|_{\xi=0} = \frac{\partial U_C}{\partial \xi}\Big|_{\xi=0} = \frac{\partial U_T}{\partial \xi}\Big|_{\xi=0} = \frac{\partial U_D}{\partial \xi}\Big|_{\xi=0} = \frac{\partial U_N}{\partial \xi}\Big|_{\xi=0} = 0 \tag{4.8}$$

According to Eq. (2.18), the tumor radius $R(t)$ evolution in time is given by:

$$\begin{cases} \dot{R}(t) = \dfrac{dR}{dt}(t) = -W_T \dfrac{1}{R(t)} \dfrac{\partial U}{\partial \xi}\Big|_{(\xi=1,t)} = -W_T \dfrac{1}{R(t)} \dfrac{\partial}{\partial \xi}(U_T + U_D + U_C + \hat{U}_C)\Big|_{(\xi=1,t)} \\ R\big|_{t=0} = R_0 \end{cases} \tag{4.9}$$

Description of the numerical algorithm:

- The "inner" domain $0 \le \xi \le 1$ and the "outer" domain $1 \le \eta \le 2$ are each discretized using equally spaced meshes; the interface is a mesh point, corresponding both to $\xi = 1$ and $\eta = 1$.

- The interface motion equation (4.9) is discretized using forward differencing in time and second order backward differencing in space (since the global cell density $U = U_T + U_D + U_C + \hat{U}_C$ is discontinuous across the interface); therefore, the new location of the interface at the current time step is obtained by using the location of the interface at the previous time step and the global cell density at the previous time step.
- The "inner" set of model governing equations (4.5) is discretized at all the internal mesh points using forward differencing in time and regular second order centered differences in space both for the second order and for the first order derivatives; similarly for the "outer" set (4.6); thus, the new values of the model state variables at the current time step are determined at all internal mesh points – both inner and outer. To update the current values of the state variables at the interface – which is both an "inner" mesh point and an "outer" mesh point, the matching conditions (4.7) are first used to determine the current values of U_A and U_C respectively at the interface; once the value for U_C is known at the current time step, then the model boundary conditions (2.16) are used to update the values of U_T and U_N at the interface at the current time step.

The implementation of the above algorithm is straightforward; the numerical stability and ultimately the convergence of the explicit method depends on the choice of the model parameters. More comments follow in the results section 4.3.

4.2 A level set (Eulerian) solution approach

The detailed description of the numerical algorithm for the fixed Cartesian mesh/level set approach in two dimensions and arbitrary geometries is addressed in Section 5 and Appendix A. The same general formulation holds regardless of the number of spatial dimensions (1,2 or 3). Below the formulation is outlined for the spherically symmetric case; this is done from a computational perspective for comparison purposes and to assess the applicability of the proposed computational methodology for the current complex tumor growth model.

As in section 4.1 above, symmetry conditions are employed at the tumor center $r = 0$.

As previously, continuity of u_A and u_C and of the related fluxes across the tumor boundary $r = R(t)$, which here translates into the continuity of U_A, U_C, $\frac{\partial U_A}{\partial r}$ and $\frac{\partial U_C}{\partial r}$ at $r = R(t)$, shall also be employed.

Description of the numerical algorithm:

- The entire fixed computational domain $0 \le r \le R_D$ is discretized using equally spaced meshing; the interface $r = R(t)$ in this case is generally not a mesh point.
- The new location of the interface at the current time step is given by the zero level set function at the current time step; the level set equation (3.3) in this case reads:

  $$\frac{\partial \varphi}{\partial t} + F\left|\frac{\partial \varphi}{\partial r}\right| = 0 \tag{4.10}$$

  where *F* is the extended velocity field, here extended off the tumor boundary such that it is constant on normal rays to the tumor boundary; as a consequence of the spherical symmetry, the extended velocity everywhere is then taken equal to the normal velocity of the tumor boundary:

$$F = -W_T \frac{\partial U}{\partial r}\Big|_{r=r(T)} \tag{4.11}$$

The initial level set function is given by $\varphi(r, t=0) = r - R_0$. To update the time-dependent level set function φ, a simple explicit first order scheme in time (forward Euler) and space is used to discretize the level set equation (4.10) (refer to Section 5 for more information). The spatial derivative in (4.11) is approximated using second order backward differencing ($U = U_T + U_D + U_C + \hat{U}_C$ is discontinuous across the interface). With the level set function updated, the new location of the interface is estimated as the zero level set by linear interpolation of the new level set function.

- The set of model governing equations (4.3) is discretized using forward differencing in time and regular second order centered differences in space both for the second and for the first order derivatives at all the internal mesh except the ones adjacent to the boundary. At points adjacent to the boundary, the spatial discretization must be modified to take into account the location of the boundary and the model prescribed boundary conditions. As already mentioned, this is accomplished by constructing local second order interpolating polynomials for each of the model dependent variables U_A, U_C, U_T, U_D and U_N respectively; then their second order derivative at a point adjacent to the boundary is approximated as the second order derivative of the corresponding polynomial; similarly for the first order derivatives.

To update the current values of the state variables at the interface – which are to be used at the next time step in constructing the local second order interpolating polynomials at points adjacent to the boundary - the continuity of U_A, U_C, $\frac{\partial U_A}{\partial r}$ and $\frac{\partial U_C}{\partial r}$ at the tumor boundary is first used to determine the current values of U_A and U_C respectively at the interface; once the value for U_C is known at the current time step, then the model boundary conditions (2.16) are used to update the values of U_T and U_N at the interface at the current time step.

Details can be found in Appendix A.

4.3 Numerical results

4.3.1 Numerical results from a computational point of view

The first aspect to be addressed is the usage of centered finite differences to approximate the first order derivatives in equation (4.3). If an heuristic stability assessment is conducted for each of the model equations (2.12) and (2.15) considered separately [30], then potential stability problems may arise if the advection terms dominate diffusion terms. An estimate for the magnitude of the relevant model parameters is necessary to fully access the stability. For the parameters considered here, the diffusion type constraint on the time-step imposed by the first equation in (2.12) will generally dominate the advection-diffusion type constraint for the second equation in (2.12). Under these conditions, the use of centered finite differences in approximating the first order derivatives is relatively safe. Numerical experiments support this conclusion. However, to investigate model behavior in regimes characterized by drift coefficients (e.g., W_C) substantially larger than the model diffusion coefficients, then upwind schemes must be used to discretize the first order spatial derivatives in the second equation (2.12).

A second aspect of computational concern is the treatment of the terms involving the Heaviside function in the first and second equation (2.15). It is common to smear out the Heaviside function for computational implementation purposes by defining:

$$H(u) \approx \frac{1}{2}(1+\frac{2}{\pi}\arctan(\frac{u}{\varepsilon})) \tag{4.15}$$

with ε a small value (typically, $\varepsilon = O(h)$, where h represents the spatial mesh size). However, in our numerical experiments performed so far, by comparing the results obtained using the actual Heaviside function and the smeared out version given by (4.15), no significant differences were detected.

Another important aspect is the choice of the larger fixed computational domain – because of the boundary conditions (2.13). In the spherically symmetric case (i.e., 1D), it is easy to employ a radius for the fixed outer domain considerably larger than the initial radius of the tumor – such that both the density of TAF U_A and the density of the new capillaries U_C naturally decay to zero towards the outer domain boundary. In higher dimensions, the choice of the domain size for the outer environment is more restricted. Numerical tests performed in the spherically symmetric case (and in 2D) have demonstrated the requirements on the choice of the outer boundary location.

Fig.1 shows a comparison between the tumor radius in time obtained via the pseudo-Lagrangian method described in section 4.1 and the tumor radius in time obtained via the

Eulerian/level set method described in section 4.2 for the following choice of the model parameters (2.19):

$$
\begin{aligned}
&K_A = 10,\ K_C = 1,\ K_N = 0.2\\
&W_C = 5,\ W_T = 10\\
&\Gamma_C = 100\\
&\Delta_A = 0.01,\ \Delta_C = 0.01,\ \Delta_T = 5,\ \Delta_N = 10,\ \Delta_D = 0.001 \qquad (4.16)\\
&\overline{U}_C = 1,\ \hat{U}_C(r) = \begin{cases} 0.1, \text{ } if \quad 3.5R_0 < r < 4R_0 \\ 0 \quad otherwise \end{cases}\\
&\overline{U}_N = 0.8,\ \tilde{U}_N = 0.9,\ B = 1\\
&R_0 = 2,\ R_D = 10
\end{aligned}
$$

The spatial mesh size in the pseudo-Lagrangian method is $\Delta\xi = \Delta\eta = 0.02$ with a fix time-step $\Delta t = 2.66 \times 10^{-5}$, while in the Eulerian/level set method $\Delta r = 0.05$ with the time-step chosen adaptively (obeying stability restrictions). These choices for the mesh sizes, initially balances the number of mesh points inside the physical domain occupied by the tumor for the two methods (the resolution remains balanced during a reasonable portion of the tumor evolution). The results show very good agreement between the two different solution methods.

4.3.2 Numerical results from a biological viewpoint

All the results discussed in this section are obtained using the above set (4.16) of model parameters as base values. Any parameter variation is explicitly defined when presenting the results.

i. *Evolution of the tumor radius in time*

In Fig.1 two different stages of tumor growth can be clearly distinguished: up to time $t \approx 1.84$, the growth is linear, at a relatively low rate – corresponding to the avascular stage; at later times, the growth is accelerated, exhibiting exponential trends – corresponding to the vascular stage. Fig. 2 shows the behavior of the tumor radius in time in the absence of tumor-induced angiogenesis, for two different values of Δ_D: the solid line corresponds to a value of $\Delta_D = 0.001$ and the dashed line to $\Delta_D = 1$; the rest of the model parameters are as in (4.16) above. In the case of the large disintegration rate $\Delta_D = 1$ for the tumor dead cells, the tumor radius shows stabilization to a limiting value of $R \approx 3$ around time $t = 10$, while in the case of the small disintegration rate $\Delta_D = 0.001$ approach to a stabilized state is not yet apparent up to time $t = 20$. This is in good agreement with the argument made in [11], that ultimately a balance between the living tumor cells and the dead tumor cells – reached when the proliferation of cells near the tumor surface balances the disintegration of dead cells in the necrotic region – determines a stationary radius of the avascular tumor. For the same value of the drift coefficient W_T, smaller values of Δ_D lead to a larger stationary radius of the tumor and a larger necrotic core with respect to the proliferation rim.

ii. *Tumor living and dead cell density evolution*

Fig. 3 plots the tumor living cell density U_T versus the radial coordinate r at various moments in time. The avascular and the vascular stages of growth are clearly differentiated here as well; in the avascular phase, U_T decreases towards the center of the tumor because the living tumor cells start to gradually die when they lack nutrients – this is confirmed by the corresponding evolution of the dead tumor cell density shown in Fig. 4; further, in the vascular phase, it is observed that the living tumor cell density continues to rapidly drop towards the center – while the dead cell density, U_D, there remains stationary (note that the model assumes dead tumor cells do not move). In the model, living tumor cells towards the center stop dying, and migrate towards less populated areas where they have a higher probability to survive and eventually continue the mitosis process if the levels of nutrients are high enough. In Fig. 6, the overall cell density, $U = U_T + U_D + U_C + \hat{U}_C$, is plotted at specific times; the curves show that once the new capillaries penetrate the tumor and begin to influence its center there will be a rapid increase of the overall cell density. Since the tumor size is relatively small here and the upper threshold for the new capillaries is high, while their death coefficient is much smaller than the growth coefficient, this happens relatively fast. The rapid increase in overall cell density leads to sharper local gradients, that in turn lead to fast movements of the living tumor cells towards the outer tumor region; in particular, there is a significant increase in the slope of the overall tumor cell density at the boundary of the tumor. Recall from Eqn (2.18) that the velocity of the tumor boundary is directly proportional to the gradient of the overall cell density.

iii. New capillary cell evolution

The evolution of the new capillaries is depicted in Fig.5. To facilitate the simulation, a large value for the growth coefficient Γ_C was chosen while the death coefficient Δ_C is small. In addition, the drift coefficient, W_C, is five times larger than the diffusion coefficient, K_C. These parameters yield significant movement of the new capillaries towards the source of angiogenic stimulus (TAF), which is maximum inside the domain occupied by the tumor. In the model, the density of new capillaries is allowed to reach an upper threshold $\overline{U}_C = 1$, which is the close packing density for the overall cell density, so the resulting scenario is not totally realistic. However, the choice of parameters related to the growth of new capillaries (which is, in fact, the core of the tumor vascularization problem) allows for the overall development of visible and meaningful changes over a relatively short period of time.

iv. The TAF and nutrient concentration evolution

The TAF distribution along the radial coordinate at various times is shown in Fig. 7. In the present version of the model, it is assumed that the living tumor cells constantly produce and release TAF, which diffuses at the same constant rate both inside the tumor and in the surrounding outer environment. Because of this assumption and the fact that the TAF decay parameter is chosen small ($\Delta_A = 0.01$) for the case considered, the evolution equation for TAF (the first equation (2.12)) is a linear diffusion equation with a source term with vanishing boundary conditions. As a result, the TAF concentration maintains a maximum at the tumor center.

The nutrient evolution is presented in Fig.8. Fig.8(a) shows the radial distribution of the nutrient at various times during the avascular phase. The nutrient reaching the tumor surface diffuses inside the tumor;. Since the evolution equation for the nutrient inside the tumor (the last equation (2.15)) is a diffusion equation with a sink term, the levels of nutrient maintain a maximum at the tumor boundary and gradually decrease towards the tumor center. As a consequence, living tumor cells first start dying at the center, while a layer of cells adjacent to the boundary are able to proliferate. Fig.8(b) shows the nutrient evolution at later times, in the vascular phase; with the accelerated development of new capillaries, increased amounts of nutrients reach the tumor surface and diffuse inside the tumor at a rate increasing proportionally to the new capillary density. This explains why the tumor dead cell density remains almost stationary from a point on (the level of nutrient becomes sufficient for the remaining living cells).

5. Description of the general numerical algorithm and discretization procedures

5.1 Construction of the "extension velocity" field off the interface

One way of extending the normal velocity off the interface in the level set equation (3.3) is extrapolation in the normal direction, following characteristics that flow outward from the interface, such that the velocity is constant on rays normal to the interface. This method, introduced by Malladi, et al. [23] works particularly well when no other information is available except for what is known on the interface–as is the case here. At points adjacent to the interface, on each side, the "extension velocity" field F is first constructed as follows: standing at a grid point adjacent to the interface, either inside the domain occupied by the tumor or outside, locate the closest point on the interface whose velocity is given by Eq. (2.18) – with second order backward differencing in the normal direction used to numerically approximate the normal derivatives – and copy its velocity. Construction of the extension velocity field in this manner has the advantage that it tends to preserve the signed distance function during the interface evolution in time. A fast way of building these extension velocities in the context of Dijkstra's-like algorithms was provided by Adalsteinsson and Sethian in [2]. An alternate way to formulate this construction is by employing a pair of linear Hamilton-Jacobi equations [26], in which the velocity values at the adjacent points are subsequently kept fixed and framed as boundary conditions for the following:

$$\frac{\partial F}{\partial \tau} + \vec{n} \bullet \nabla F = 0 \;\; in \;\; \Omega^{out}(t) \tag{5.1}$$

$$\frac{\partial F}{\partial \tau} - \vec{n} \bullet \nabla F = 0 \;\; in \;\; \Omega(t) \tag{5.2}$$

where the local unit outward normal in the level set methodology is defined everywhere as:

$$\vec{n} = \vec{n}(\vec{x}, t) = \frac{\nabla \varphi(\vec{x}, t)}{\left| \nabla \varphi(\vec{x}, t) \right|} \tag{5.3}$$

Here τ designates a pseudo-time for the relaxation of the equations to steady-state at each moment of time t. Equations (5.1) and (5.2) are numerically discretized using a regular first order upwind scheme [22],[26] and iterated to steady-state, where the corresponding solution $F = F(\vec{x}, t)$ will be constant on rays normal to the interface.

The normal $\vec{n} = \vec{n}(\vec{x}, t)$ in (5.3) is approximated using the construction described in [31]; the local unit outward normal at a point on the interface - which generally is not a grid point - is obtained by bilinear interpolation from the values of the local unit outward normal computed at the four neighboring nodes on the fixed Cartesian grid.

5.2 Re-initialization of the level set function φ

As discussed by Chopp [13], in general, a procedure is needed to reset the level set function φ as a signed distance function to the interface (in this case, the tumor boundary) from time to time. Re-initialization at some moment of time t can be regarded as the process of replacing the current level set function $\varphi(\vec{x},t)$ by another function $\varphi^{reinit}(\vec{x},t)$ that has the same zero contour but is better behaved; $\varphi^{reinit}(\vec{x},t)$ becomes the new level set function to be used as initial data until the next re-initialization. Reinitialization and its role in Narrow Band Methods was first analyzed in depth by Adalsteinsson and Sethian in [2], and a very fast Dijkstra-like method to perform this reinitialization was given by Sethian in [34].

Another way of re-initializing the level set function φ to a signed distance function to the interface employs the following “re-initialization equations” [26]:

$$\frac{\partial \varphi^{reinit}}{\partial \tau} + (\left|\nabla \varphi^{reinit}\right| - 1) = 0 \qquad in\ \Omega^{out}(t) \tag{5.4}$$

$$\frac{\partial \varphi^{reinit}}{\partial \tau} - (\left|\nabla \varphi^{reinit}\right| - 1) = 0 \qquad in\ \Omega(t) \tag{5.5}$$

with

$$\varphi_0^{reinit} = \varphi^{reinit}(\vec{x}, \tau = 0) = \varphi(\vec{x}, t) \tag{5.6}$$

Here again, τ designates a pseudo-time for relaxing the equation to steady-state at a fixed real time t. As before in the case of the extension velocity, first at grid points adjacent to the boundary, on each side, φ^{reinit} is reset close to a signed distance function by hand (a very efficient way is the initialization stage of the fast marching method in [31]). These values are subsequently kept fixed and framed as boundary conditions for the equations (5.4) and (5.5) respectively, that are individually solved to steady-state. The resulting solution $\varphi^{reinit}(\vec{x}, t)$ will be a signed distance function to the interface $\Sigma = \Sigma(t)$ at the particular time t in the model evolution.

The implementation of the level set methodology is presented here for the two-dimensional case, but the extension to three dimensions is straightforward. The domain occupied by the tumor Ω is embedded into a larger fixed, time-independent, computational domain **D**, that is discretized using a uniform Cartesian mesh with $\Delta x = \Delta y = h.$ The region outside of the tumor is denoted by $\Omega^{out} = \mathbf{D} \setminus \Omega$. The tumor boundary will also be referred to as the "interface" – separating the domain occupied by the tumor from the outside tissue. A "regular" grid point (either inside the domain occupied by the tumor or outside) shall denote a point on the fixed Cartesian grid that has no neighbors on the tumor boundary, in either the horizontal (x) direction or the vertical (y) direction, while an "irregular" grid point (on each side of the tumor boundary) corresponds to a point on the fixed Cartesian grid that is adjacent to the boundary, either horizontally or vertically.

5.3 Discretization of the level set equation and the re-initialization equation

The level set equation (3.3) is discretized using a conservative scheme for nonlinear Hamilton-Jacobi equations with convex Hamiltonian [31]:

$$\varphi_{i,j}^{n+1} = \varphi_{i,j}^{n} - \Delta t[\max(F_{i,j}^{n},0)\nabla^{+} + \min(F_{i,j}^{n},0)\nabla^{-}] \tag{5.7}$$

where:

$$\varphi_{i,j}^{n} = \varphi(x(i), y(j), n\Delta t)$$
$$F_{i,j}^{n} = F(x(i), y(j), n\Delta t)$$
$$\nabla^{+} = [\max(D^{-x}\varphi_{i,j}^{n},0)^{2} + \min(D^{+x}\varphi_{i,j}^{n},0)^{2} + \max(D^{-y}\varphi_{i,j}^{n},0)^{2} + \min(D^{+y}\varphi_{i,j}^{n},0)^{2}]^{\frac{1}{2}} \tag{5.8}$$
$$\nabla^{-} = [\max(D^{+x}\varphi_{i,j}^{n},0)^{2} + \min(D^{-x}\varphi_{i,j}^{n},0)^{2} + \max(D^{+y}\varphi_{i,j}^{n},0)^{2} + \min(D^{-y}\varphi_{i,j}^{n},0)^{2}]^{\frac{1}{2}} \tag{5.9}$$

and D^{-x} (D^{-y}) stands for the backward differencing approximation of the first-order partial derivative in the x (y)–direction, while D^{+x} (D^{+y}) stands for the forward differencing approximation. The above scheme is a first order (forward Euler) in time; higher order schemes such as HJ ENO or WENO can be employed [26]. The time step in (5.7) must obey the CFL condition for stability:

$$\Delta t \max_{i,j}\left|F_{i,j}^{n}\right| \le \frac{h}{2} \tag{5.10}$$

A similar scheme is used to discretize the re-initialization equations (5.4) and (5.5).

5.4 Overall numerical solution procedure

The governing model equations are discretized using explicit finite difference schemes, which enables straightforward implementation. Details of the numerical solution procedure for the model dependent variables are given in Appendix A. A comparison of spatial discretization schemes for the level set equation and a discussion of the approximation error is given in [17]. Here, the global solution algorithm is outlined briefly in terms of the following steps:

1) It is assumed that all the model dependent variables: $U_A(\vec{x},t)$, $U_C(\vec{x},t)$, $U_T(\vec{x},t)$, $U_D(\vec{x},t)$, $U_N(\vec{x},t)$ (all initially given by the model initial conditions (2.14) and (2.17)) along with the level set function $\varphi(\vec{x},t)$ are known at time t, with the level set function equal to the signed distance function (prescribed initially, or as a result of re-initialization at later times). As a result, the current location of the interface is implicitly known. Following [1], a "narrow band" (tube) is built around the interface, with a user-prescribed width. Since $\varphi(\vec{x},t)$ is assumed close to a signed distance function, the narrow band is defined by locating the points using the following criterion:

$$\left\{\vec{x} \,\middle|\, |\varphi(\vec{x},t)| < width\right\} \overset{not.}{=} T \,.$$

The grid points inside the tube and the grid points near the tube edge are marked distinctly.

2) With the value of $U(\vec{x},t) = U_T(\vec{x},t) + U_D(\vec{x},t) + U_C(\vec{x},t) + \hat{U}_C(\vec{x})$ known at the time step t, the "extension velocity" field $F = F(\vec{x},t)$ is constructed as described in Section 5.1, at points $\vec{x}$ inside the narrow band tube T .

3) With the extension velocity field computed at points inside the tube T, the level set equation (5.7) is solved inside the tube to update the level set function at the next time step. The values of the level set function at grid points distinctly marked near the tube edge in Step 1 are frozen, as well as the values of the level set function outside the tube T. The following conditions are monitored:

a) whether the newly updated tumor boundary (interface) approaches the tube edge to within a specified tolerance (if so, then the values kept frozen in Step 4, which serve as artificial numerical boundary conditions, will severely affect the actual location of the interface);

b) whether steep or flat gradients are developing in the newly updated level set function, particularly at points neighboring the interface.

4) With the new location of the boundary implicitly captured by the updated level set function $\varphi(\vec{x}, t+\Delta t)$, the model governing Eqs. (2.12) and (2.15) along with the corresponding prescribed boundary conditions (2.13) and (2.16) are employed to compute the new values of the model dependent variables: $U_A(\vec{x}, t+\Delta t)$, $U_C(\vec{x}, t+\Delta t)$, $U_T(\vec{x}, t+\Delta t)$, $U_D(\vec{x}, t+\Delta t)$, $U_N(\vec{x}, t+\Delta t)$ as described in Section 5.4 .

Steps 2-4 are repeated until either situation a) or b) occurs; when this happens, the narrow band (tube) T must be rebuilt and the procedure begins with Step 1 again. Employing this narrow band level set method is computationally very efficient (especially in constructing the extension velocity field); this approach is ideal when only the evolution of the interface itself is of interest (i.e., the zero level set), as is the case here.

6. Numerical results in two dimensions – arbitrary geometry

6.1 Computational Details

The numerical simulations presented here were obtained by employing straightforward finite-difference schemes. The motivation was to create a framework that could be easily implemented to study a variety of tumor growth models. For the present model, since no curvature effects at the tumor boundary are incorporated, we find that a first-order spatial scheme in the level set equation (5.7), as well as in the re-initialization equations (5.4), (5.5) can be safely used. For the same reason, the size of the narrow band (tube) T can be relatively modest – here a width of $6h$ on each side of the interface is chosen and the interface is only allowed within at most 2 grid cells from the tube boundary (i.e., it is allowed to move at most 4 grid cells within the tube) before the tube is rebuilt. As in [17], re-initialization is typically used jointly with re-building the narrow band. They also determined that the forward Euler time integration scheme for the level set equation (5.7) was sufficient; particularly since the time step is small due to the overall fully explicit nature of the solution procedure.

Regarding the choice of the “small” value ε in the ε-test (see Eq. (A.5) in Appendix A), since the actual location of a boundary point is found by linear interpolation of the level set function at the neighboring grid points, one natural consistent choice for ε is

$\varepsilon \sim O(h^2)$; the results in the spherically symmetric case via the Eulerian/level set approach in Section 4 are obtained by using $\varepsilon = h^2$. However, this choice is related strictly to the spatial accuracy of the numerical approximation, and has no apparent geometrical interpretation; in the context of Eq. (A.5), the geometrical location of a boundary point (either in the horizontal or in the vertical direction) is in-between two Cartesian grid points, and the actual measure of how close one of the two grid points is to the boundary point is given by a fraction of the grid size h. In our numerical experiments we found that a good choice for ε is $\boldsymbol{\varepsilon = h / N}$, with N an integer that depends on the geometrical properties of the front involved. If no curvature effects are present – as in the current model – then $\boldsymbol{\varepsilon = h} / 5$ was found to work well. This is demonstrated by the results shown in Fig. 9, where the initial tumor boundary is taken to be a circle centered at the origin with radius 1, and the support of pre-existing capillaries is a circular area surrounding the initial tumor: $S = \{(x, y) \mid 2 < \sqrt{x^2 + y^2} < 2.3\}$. The set of model parameters (4.16) is used, but with the pre-existing capillary density taken five times larger, to speed up the calculations ($\hat{\boldsymbol{U}}_{\boldsymbol{C}} = 0.5$ inside S). A comparison is performed between the tumor radius evolution obtained by three different sets of calculations: the two-dimensional Cartesian level set approach described in Section 5, the one-dimensional Eulerian/level set approach described in Section 4.2 (under the assumption of polar symmetry) and the one-dimensional pseudo-Lagrangian method described in Section 4.1 under the assumption of polar symmetry as well. For the 2D method, the fixed Cartesian mesh size is $h = 0.05$, the computational domain (outer environment) is $[-4,4] \times [-4,4]$ and the time step is adaptive; in the 1D Eulerian/level set method, the mesh size is

$\Delta r = 0.05$, the radius of the outer environment is $R_D = 4$ and the time step is adaptive; in the 1D pseudo-Lagrangian method, the mesh size is $\Delta\xi = \Delta\eta = 0.04$ and the time step is $\Delta t = 6.4 \times 10^{-5}$. The results demonstrate that the two-dimensional problem formulated in Cartesian coordinates in this case exhibits genuine polar symmetry while in the avascular phase of the tumor growth (see model equations (2.15) – (2.17)), but it gradually starts to depart from it with the increased development of new capillaries in the subsequent vascular phase. This is due to the geometric computational configuration of the outer environment in Cartesian coordinates, which is a fixed square box, and not a circle (how long the assumption of full polar symmetry can be employed depends on the size of the fixed Cartesian computational box relative to the tumor radius). There is very good agreement for the growth rate between the three sets of results up to time $t \approx 0.5$ (which corresponds to the avascular phase of growth); the agreement continues to be good (within the overall accuracy of the methods) up to time $t \approx 0.9$. Eventually, the two-dimensional Cartesian result no longer compares to the one-dimensional results obtained under the assumption of full polar symmetry.

Similarly with the argument made in [17], when computing the normal velocity of the tumor interface via Eq. (2.18), a second-order accurate backward difference approximation in the normal direction is found optimal here as well. If the field variables U_T, U_D and U_C are numerically computed with second-order spatial accuracy, then the numerical estimate of the normal velocity of the interface can only be at most first-order accurate. Thus, it is to be expected that the location of the tumor boundary can be found at most with first-order spatial accuracy.

All the results that follow are obtained within the framework of the general Eulerian level set/Cartesian grid methodology described in Section 5 above. In Fig. 10, the results of a convergence study are shown. The tumor initial boundary is given by the 4-fold symmetrically perturbed circle:

$$(x(\alpha), y(\alpha)) = (4.8 - 0.4\cos(4\alpha + \frac{\pi}{4}) - 0.4\sin(4\alpha + \frac{\pi}{4}))(\cos(\alpha), \sin(\alpha)),\ \alpha \in [0, 2\pi] \quad (6.1)$$

The same model parameters as in Fig. 9 above are used. Outside the domain occupied initially by the tumor there are four fixed circular seeds of pre-existing capillaries, symmetrically positioned and relatively close to the boundary of the outer environment. This initial configuration will be described in more detail below. The evolution of the tumor boundary computed using three different mesh sizes: $h = 0.4$, $h = 0.2$ and $h = 0.1$ is shown at three different moments of time and the qualitative convergence can be observed. The mesh sizes were chosen to allow for two levels of refinement, starting with a reasonable mesh spacing. Currently, the methodology developed here is designed for implementation on moderately sized, standalone computing platforms. Moderate mesh resolution, relative to the initial tumor size, was used to evaluate the solution behavior and determine whether the results show the correct qualitative trends.. Through numerical testing, it was found that the location of the tumor boundary was not very sensitive to the spatial mesh size, when the value of the drift coefficient W_T equal to 10 or smaller, since there is no curvature effect at the boundary in the current model. In [17], where the tumor boundary curvature was important, for drift coefficients of the same order of magnitude, considerable sensitivity to the spatial resolution was found.

The accuracy of the tumor boundary location in time can be quantitatively estimated [17]. The level set method reconstructs the interface at every moment of time as a piecewise linear manifold; suppose that the Cartesian mesh size is doubled twice and denote by $\{\vec{x}^{n,1}_{\mathrm{int}erface,k}\}\big|_{k=\overline{1,N_1}}$, $\{\vec{x}^{n,2}_{\mathrm{int}erface,k}\}\big|_{k=\overline{1,N_2}}$ and $\{\vec{x}^{n,4}_{\mathrm{int}erface,k}\}\big|_{k=\overline{1,N_4}}$ the collection of interface points

$\vec{x}^{n}_{\mathrm{int}erface,k} = (x_{\mathrm{int}erface,k}, y_{\mathrm{int}erface,k})$ at time $t = t_n$ corresponding to the coarsest mesh, the intermediate mesh and the finest mesh, respectively. Thus, the interface is represented as a polygonal line with N_1, N_2 and N_4 line segments for the coarsest, intermediate and finest representation, respectively. Each polygonal line can be re-divided into the same given number N of equally spaced points (typically $N = N_4$) and the newly determined points on each polygonal line are correspondingly marked as $\{\vec{X}^{n,1}_{\mathrm{int}erface,k}\}\big|_{k=\overline{1,N}}$, $\{\vec{X}^{n,2}_{\mathrm{int}erface,k}\}\big|_{k=\overline{1,N}}$ and $\{\vec{X}^{n,4}_{\mathrm{int}erface,k}\}\big|_{k=\overline{1,N}}$, respectively.

Since no analytic solution is available, the errors are computed with respect to the numerical solution corresponding to the finest mesh $\{\vec{X}^{n,4}_{\mathrm{int}erface,k}\}\big|_{k=\overline{1,N}}$; following [18], the error at time $t = t_n$ is defined as the largest Euclidean distance of the corresponding points of the two computed interfaces:

$$e^{n}_{4\_1} = \max_{k=\overline{1,N}} \left| \vec{X}^{n,1}_{\mathrm{int}erface,k} - \vec{X}^{n,4}_{\mathrm{int}erface,k} \right| \tag{6.2}$$

$$e^{n}_{4\_2} = \max_{k=\overline{1,N}} \left| \vec{X}^{n,2}_{\mathrm{int}erface,k} - \vec{X}^{n,4}_{\mathrm{int}erface,k} \right| \tag{6.3}$$

A ratio $e^n_{4\_1}/e^n_{4\_2}$ between 4 and 5 typically indicates second-order spatial accuracy, while a ratio between 2 and 3 typically indicates first-order spatial accuracy [18]. The quantitative errors resulting from the mesh refinement analysis in Fig. 11 are recorded in Table 1. According to these values, the tumor boundary location using the fixed Cartesian mesh, ”narrow band” level set approach developed here is found with first-order spatial accuracy during its evolution in time.

Table 1.

time	$e^n_{4\_1}$ (6.2)	$e^n_{4\_2}$ (6.3)	$\frac{e^n_{4\_1}}{e^n_{4\_2}}$
t=0.353	0.0584	0.0319	1.83
t=0.8236	0.1263	0.0614	2.058
t=1.1766	0.2839	0.1036	2.74

6.2 *Model Behavior*

As discussed in Section 4.3.2, the numerical results presented for both the spherically symmetric and two-dimensional cases correspond to computationally optimal conditions for the tumor vascularization (i.e., increase in new capillary density) as predicted by the model. The model parameters (2.19) chosen for the simulations here enable readily visible and significant changes in the tumor growth process over a relatively short period of time. For more moderate choices of these parameters (particularly in the equation for the new capillary density), the current model yields long and slowly evolving avascular stages of growth, before the tumor begins to develop its own capillary network. During the avascular stage the growth is stable, with a linear rate of growth initially, that decreases asymptotically to zero. It is the vascularization of the tumor via the tumor induced angiogenesis contained in the model that leads to more rapid and unbounded growth. From a computational standpoint, the stability requirements due to the fully explicit nature of the numerical scheme lead to certain practical bounds on the choice of the model parameters used in the actual simulations.

For the 2-D simulation results presented in Figs.11 and 12, the same set of model parameters used for the case shown in Fig. 9 was used. In Fig. 11(a), the evolution of the tumor with the initial boundary given by Eq. (6.1) is shown in detail. Outside the domain occupied initially by the tumor there are four circular seeds of pre-existing capillaries, symmetrically positioned and relatively close to the boundary of the outer environment; their location is marked by the small gray circles, of centers: (6,6), (-6,6), (-6,-6) and (6,-6) respectively, and radius 1.2; the Cartesian mesh size $h = 0.1$, the computational domain (outer environment) $[-8,8] \times [-8,8]$ and the time step is adaptive. The initial tumor boundary is deliberately chosen as a circle symmetrically perturbed towards the location of the pre-existing capillaries. Up to time $t \approx 0.6$ the tumor is in the avascular phase–the growth is very slow, stable and self-similar. At time $t \approx 0.9$, corresponding to an intermediate to moderate degree of tumor vascularization, instability starts to become evident as the initially perturbed tumor boundary grows more towards the location of the pre-existing capillaries, exhibiting a tendency to elongate. However, at later times, in a high vascularization phase, the elongation is less apparent and the tumor continues to expand rapidly but in a relatively uniform manner. The explanation of the growth behavior is found in the corresponding evolution of the new capillaries, depicted in Fig.

11(b), where both a contour map(11b-1) and a surface plot(11b-2) of the new capillary density are included. It can be seen that the endothelial cells stimulated initially are the ones belonging to the pre-existing capillaries. At early times, since the new capillaries have not evolved sufficiently to reach the tumor, it remains in the avascular phase and the slow stable growth occurs as described above. An intermediate stage of vascularization follows when enough new capillaries have developed outside the tumor in the regions neighboring the location of the pre-existing capillaries, such that they undergo a strongly oriented movement towards the source of angiogenic stimulus – the tumor itself. It is in this stage that the tumor exhibits the tendency to elongate towards the location of the pre-existing capillaries. At later times, once the newly formed blood vessels (characterized by the capillary density) have reached inside the tumor, they are in turn stimulated to proliferate, and a faster tumor vascularization follows (due to the fact that the TAF values are much higher inside the tumor than outside, coupled with the large value of the growth coefficient, $\Gamma_C = 100$). Eventually, the new capillary distribution tends to level-off spatially leading to subsequent quasi-uniform growth of the tumor.

Contour maps of the tumor living cell density are shown in Fig. 11(c). In the avascular phase of the tumor growth, a rim structure develops as described in [11]. The results show a very thin outer rim of proliferative cells, followed by a slightly thicker adjacent rim of quiescent cells–cells that live but do not proliferate. The inner tumor region shows a smooth transition towards a large necrotic core. The choice of the nutrient threshold values $\overline{U}_N = 0.8 < \tilde{U}_N = 0.9$ in (4.16) allows for the existence of a quiescent rim of living tumor cells (a tumor region where the nutrient levels reaching the existent living cells are such that $\overline{\boldsymbol{U}}_{\boldsymbol{N}} < \boldsymbol{U}_{\boldsymbol{N}} / \boldsymbol{U}_{\boldsymbol{T}} < \tilde{\boldsymbol{U}}_{\boldsymbol{N}}$). The smooth transition towards a large necrotic core is confirmed by the evolution of the tumor dead cells shown in Fig. 11(d).

The distinct patterning in the living and dead cell densities at later times results from the development and the subsequent spatial distribution of the new capillaries. A local increase of the new capillary density affects the value of the living cell density on the tumor boundary due to the given boundary conditions. Inside the tumor, local gradients of the overall cell density U develop and the living tumor cells are redistributed accordingly. The pattern of the living tumor cells in turn impacts the pattern of the dead cells; moreover, since the disintegration coefficient of the dead cells in these simulations is taken very small ($\Delta_D = 0.001$), the dead cells subsequently continue to have an important contribution to the overall cell density U From the evolution equations for the living and dead cell density, if enough cells die in a certain area, then the nutrient may be sufficient for the remaining living cells.

Fig. 11(e) shows contour maps of the TAF concentration level. As in the 1-D case, it has a maximum at the tumor center and decreases rapidly at the outer boundary of the tumor (refer to the comments in the spherically symmetric case). Finally, in Fig. 11(f) contour maps of the nutrient distribution inside the tumor are shown. Because significant amounts of nutrient are consumed by the living tumor cells adjacent to the tumor boundary, the nutrient level decreases considerably towards the central region, which leads to the large area of dead cells in the center region of the tumor. Another notable aspect here is the manner in which the levels of nutrient reaching the tumor boundary increase with the development of new vasculature in the vascular phase of growth.

For the results presented in Fig.12, the initial configuration considered previously in Fig. 11 is geometrically scaled down by a factor of 4. Both the size of the tumor and the radius of the pre-existing capillary regions are reduced. The domain occupied initially by the tumor is given by:

$$(x(\alpha), y(\alpha)) = (1.2 - 0.1\cos(4\alpha + \frac{\pi}{4}) - 0.1\sin(4\alpha + \frac{\pi}{4}))(\cos(\alpha), \sin(\alpha)),\ \alpha \in [0, 2\pi] \quad (6.4)$$

while the four symmetric circular seeds of pre-existing capillaries (their locations marked by the four gray circles in Fig.12(a)) are located in a similar position relative to the outer domain border as in the previous case, but their center position is scaled by a factor of 4. The comparison between the two cases illustrates some interesting differences in the tumor evolution due strictly to size and geometry as predicted by the model. The same set of model parameters is used in both cases. The individual graphs in Fig.12 are organized in the same manner as Fig. 11 for comparison purposes. Fig.12(a) shows the evolution of the tumor beginning with the initial boundary given by Eq. (6.4). Up to time $t \approx 0.4$ the small tumor is in the avascular phase; around that time, as characterized by the density , U_C shown in Fig.12(b), newly formed capillaries start to reach the tumor surface. However, the new capillary density remains relatively small up to time $t \approx 0.6$ (low vascularization regime), such that in this phase the growth is very slow, stable, and remains self-similar. At later times, in the fully-developed vascular phase, the tumor expands fast in a relatively uniform manner. Unlike the previous case, the extension of the tumor boundary towards the location of the pre-existing capillaries is not apparent. An explanation can be found in the corresponding evolution of the new capillary density as depicted in Fig. 12(b), again shown both as surface plots and contour maps. The tumor size in this case is smaller, which leads to lower levels of TAF inside the tumor and, as a consequence, lower levels of TAF reaching outside to stimulate the pre-existing capillaries to proliferate (see Fig. 12(e)); therefore, the density of the new capillaries is proportionally lower. In the present case, the distances between the pre-existing capillaries locations are 4 times smaller and the tumor boundary is 4 times closer to the pre-existing capillaries. As a result, diffusion leads to a substantially more uniform spatial distribution of the new capillary density in the intermediate vascularization phase than in the previous case of the larger tumor. Since the tumor size is smaller in the second simulation example, the model illustrates how new capillaries penetrate and reach the tumor central region faster than in the first example, such that the density of the new capillaries in the high vascularization phase exhibits a visible peak at the tumor center.

The spatial distribution of the tumor living cells in the second example, Fig. 12(c), is less interesting than in the previous case. The rim of quiescent cells in this case is considerably wider relative to the tumor size than before. An examination of the evolution of the dead cell density, Fig.12(d), suggests that the same comments made in Section 4.3.2 for the spherically symmetric case regarding the evolution of the tumor cells hold here as well. The central tumor region in transition towards a necrotic core is small in this case, and much less dynamic than in the previous case for the larger tumor, where the living tumor cell density exhibits highly varying spatial re-distributions in the vascular phase, Fig. 11(c).

Finally, the following aspects are worth considering regarding the comparison between the simulations for the large tumor and its small replicate: the larger tumor expands more slowly than the smaller one during their corresponding avascular phase. This is correct from a biological viewpoint, since in the avascular phase, a tumor can only reach a certain limiting size corresponding to a quasi-equilibrium state, where a balance is eventually achieved between the tumor living and dead cells. Under identical actual growth conditions (translated here into identical model parameters and initial conditions), in the absence of vascularization, the larger tumor is expected to approach a stabilized state faster. On the other hand, once the vascular phase occurs, the model correctly predicts a subsequent tumor expansion–more aggressive in the case of the large tumor–at increasingly higher normal velocities.

Lastly, the case of an initially asymmetric tumor boundary is considered with the following initial tumor boundary:

$$\begin{aligned}(x(\alpha), y(\alpha)) = (&1 + 0.12\cos(2\alpha) + 0.1\sin(2\alpha) + 0.06\cos(3\alpha) + 0.05\sin(3\alpha) \\ &+ 0.04\cos(5\alpha) + 0.07\sin(6\alpha))(\cos(\alpha), \sin(\alpha)), \qquad \alpha \in [0, 2\pi]\end{aligned} \tag{6.5}$$

The location of the pre-existing capillaries is a disk of center (1.5,1.5) and radius 0.3. The initial profile is marked by the small dashed gray circle in Fig.13. The density of the pre-existing capillaries is constant and set at 0.4. The model parameters (4.16) were used, except for $\overline{U}_C = 0.4$ and $K_N = 10$. The Cartesian mesh size is $h = 0.1$, the computational domain (outer environment) is $[-4,4] \times [-4,4]$ and the time step is adaptive. The evolution of the tumor boundary in time is shown in Fig.13 at equal time increments of 0.25 up until time $t = 2.5$, when the support of the pre-existing capillaries has been entirely engulfed by the advancing tumor boundary. As before, the evolution of the tumor corresponding to the avascular phase is slow and stable, in self-similar shapes. At later times, in the vascular phase, the self-similarity is lost in a quasi-uniform manner.

For the final set of results presented, the effect of varying the model parameters K_N (that characterizes the dependence of the nutrient diffusion rate inside the tumor on the presence of capillaries) and Γ_C (characterizing the growth rate of the new capillaries) is investigated for the same initial tumor boundary given by Eq.(6.5). The same location and density for the pre-existing capillaries as in the previous case were used. A comparison of the tumor boundary evolution for three sets of parameter values is shown in Fig.14. The tumor boundary represented by the dotted line corresponds to the values $K_N = 10$ and $\Gamma_C = 10$, the dash-dot line to $K_N = 0$ and $\Gamma_C = 100$ and the solid line to $K_N = 10$ and $\Gamma_C = 100$. For all three cases, the tumor boundary is shown at time $t = 2.5$. The results show that the tumor boundary evolution is much more sensitive to the value of the new capillary growth coefficient than it is to the nutrient diffusion coefficient through the capillaries. Inhibiting the nutrient diffusion through the capillaries inside the tumor (by setting $K_N = 0$ as opposed to $K_N = 10$) leads to a moderate slowdown of the tumor expansion in time. By reducing the growth rate of the new capillaries one order of magnitude, a significantly higher reduction of the tumor size over time is achieved. Thus, with respect to a virtual treatment scenario (e.g., by the usage of drugs such as Angiostatin), a significant decrease of the capillary growth rate shows immediate and visible consequences on the tumor growth rate, slowing it down considerably in time.

7. Conclusions

A comprehensive multi-cell tumor growth model was successfully analyzed in detail using finite-difference solution techniques and an efficient narrow band level-set method to capture the evolution of the tumor boundary. The finite-difference discretization is particularly appropriate for this model, since the governing equations can be derived alternatively using a lattice-based approach [15] that directly yields a finite-difference type formulation. The continuum model incorporates the effect of angiogenesis in a deterministic fashion. It is well-established (Folkman, [16]), that tumor vascularization occurs through tumor-induced angiogenesis–the process where nutrient deficient living tumor cells release a chemical TAF (Tumor Angiogenic Factor). The TAF diffuses into the healthy surrounding tissue and stimulates the capillary network existent nearby outside the tumor, which leads to formation of new blood vessels through the accumulation of new endothelial cells. The new capillaries move towards the source of angiogenic factor leading to tumor vascularization. These important mechanisms associated with the angiogenesis phenomena are realistically incorporated in the present model, in a deterministic, macroscopic sense. The simulations presented both under the assumption of spherical symmetry as well as in arbitrary geometries in two dimensions confirm that the comprehensive model is able to capture both the avascular and the vascular phase of tumor growth, and to provide a quantitative tool for use in studying how and when this fundamental transition occurs. The progressive formation of a tumor necrotic core is captured as in many existing models for avascular growth, with the balance of proliferation and transport effects correctly varying according to the tumor size (large necrotic core for larger tumors, small necrotic cores for smaller ones). Moreover, the rim structure of the tumor in the avascular phase is well-exhibited, with rim size depending on the tumor size: for larger tumors, the proliferative and the quiescent rims are thin relative to the tumor size, while smaller tumors exhibit a thicker layer of quiescent cells.

While the overall behavior predicted by the model in arbitrary, two-dimensional geometries is reasonable, the model in its present form does not include effects that allow for more intricate tumor boundary evolution. Models have been developed which incorporate cell adhesion effects at the tumor boundary (Byrne and Chaplain, [7]). These models lead to a Gibbs-Thomson (or Young-Laplace) type of condition on the tumor boundary which relates the growth behavior to the curvature of the boundary. As is well known from inorganic phase boundary evolution, this type of condition leads to complex morphology in systems governed by diffusive transport. Clearly, more complex physics, soundly based on smaller-scale biological mechanisms, still needs to be incorporated in order to model tumor growth under more general conditions (e.g., conditions under which tumor boundaries exhibit “fingering” or more complex morphology). Since all the transport coefficients appearing in the model have been taken constant in the simulations so far (physically corresponding to a homogeneous, isotropic growth environment), the only potential source of “anisotropy” comes from the location of the pre-existing capillary network in the healthy tissue region neighboring the tumor. The numerical experiments so far tend to demonstrate that, while a more complicated arrangement of the pre-existing capillaries may yield more complex tumor boundary evolution in the intermediate/moderate vascularization regime, with constant transport coefficients morphological complexity is diminished in the high vascularization regime. In fact, this result is in good agreement with recent experimental results on *in vivo* tumors grown in an isotropic sponge-like matrix [14].

As far as the computational framework developed here is concerned, the advantage is its generality and relative simplicity of implementation, which makes the implementation of different model features straightforward to incorporate. The formulation details presented here and in a companion article (Hogea, et al. [17]) provide a comprehensive description of the numerical procedure implementation. In the last five years, building on work over many years, a number of detailed tumor growth models have been developed that may be valuable tools for better understanding tumor growth and specific treatment regimes when implemented computationally. In order for this type of modeling to provide useful information from a medical research prospective, mechanically and biologically realistic models will have to be used for simulations in 3-D. The methodology developed here is readily adaptable to three-dimensional calculations from an algorithmic point of view. All the components of the numerical schemes involved extend to the three-dimensional formulation in a straightforward manner (often translating to simply adding one more dimension to the arrays involved). The straightforward finite-difference procedures are well-suited for parallel implementation, which is becoming the pervasive large-scale computing platform. Moreover, the level set method in the narrow band implementation has the ability of naturally capturing potentially large topological changes in the tumor boundary evolution in time at reduced computational expense, while automatically providing information about the local geometric properties. This is crucial for simulations of complex tumor growth where different biological phenomena may occur inside the tumor and outside in the healthy surrounding tissue. More accurate and less restrictive time integration schemes are one aspect where the current implementation has to be improved. This would enable more accurate studies of the model behavior over a broader range of model parameters. These schemes are currently under development and will be incorporated in future studies.

References:

[1] Adalsteinsson D., Sethian J.A., *A Fast Level Set Method for Propagating Interfaces*, J. Comp. Phys. 118, 2, 269-277 (1995)

[2] Adalsteinsson D., Sethian J.A., *The fast construction of extension velocities in level set methods*, J. Comp. Phys. 148, 2-22 (1999)

[3] Adam J., *General aspects of modeling tumor growth and immune response*, in *A Survey of Models on Tumor Immune Systems Dynamics*, (Edited by J. Adam and N. Bellomo), 15-88, Birkhäuser, Boston, (1997)

[4] Alexiades V., *Overcoming the stability restriction of explicit schemes via super-time-stepping*, 2nd International Conference on Dynamic Systems and Applications (1995)

[5] Araujo R.P., McElwain D.L.S., *A History of the Study of Tumor Growth: The Contribution of Mathematical Modeling*, 66 (2004) 1039-1091

[6] Belomo N., Preziosi L., *Modeling and mathematical problems related to tumor evolution and its interaction with the immune system*, Math. and Comp. Model. 32 (2000) 413-452

[7] Byrne, H.M., Chaplain M.A.J., *Modelling the role of cell-cell adhesion in the growth and development of carcinomas*, Mathl. Comput. Modelling, 24, 1-17 (1996)

[8] Byrne H.M., King J.R., McElwain D.L.S., Preziosi L., *A two-phase model of solid tumor growth.* Appl. Math. Letters, (2002)

[9] Byrne H.M., Preziosi L., *Modeling solid tumour growth using the theory of mixtures*, IMA J. Appl. Med. Biol., (2002)

[10] Calhoun D., *A Cartesian grid method for solving the two-dimensional stream function-vorticity equations in irregular regions*, J. Comp. Phys. 176, 231-275 (2002)

[11] Chaplain M.A.J., Preziosi, L., *Macroscopic modeling of the growth and development of tumor masses*, preprint (2001)

[12] Chen S., Merriman B., Osher S. , Smereka P., *A Simple Level Set Method for Solving Stefan Problems,* J.Comp. Phys. 135, 8-29 (1997)

[13] Chopp D.L., *Computing Minimal Surfaces via Level Set Curvature Flow*, J. Comp. Phys. 106, 77-91 (1993)

[14] V. Cristini, J. Lowengrub and Q. Nie*, Nonlinear Simulation of Tumor Growth,*
J. Math. Biol. 46**,** 191-224 (2003)

[15] De Angelis E., Preziosi L., *Advection-diffusion models for solid tumour evolution in vivo and related free boundary problem*, Math.Mod.Meth.Appl.Sci., Vol.10, no.3, 379-407 (2000)

[16] Folkman J., *The Vascularization of Tumors,* Scientific American, May 1976

[17] Hogea C.S., Murray B.T., Sethian J.A., *Computational modeling of solid tumor evolution via a general Cartesian mesh/level set method*, submitted to J.Comp.Appl.Math.

[18] Hou T.Y., Li Z., Osher S., Zhao H., *A Hybrid Method for Moving Interface Problems with Application to Hele-Shaw flow*, J. Comp. Phys. 134 (1997)

[19] Kansal A.R., Torquato S., Harsh IV G.R., Chiocca E.A., Deisboeck T.S., *Simulated brain tumor growth dynamics using a three-dimensional cellular automaton*, J. theor. Biol. 203: 367-382 (2000).

[20] Kim Y., Goldenfeld N., Dantzig J., *Computation of Dendritic Microstructures using a Level Set Method,* Phys. Rev. E, 62, 2, 2471-2474 (2000)

[21] LeVeque R.J., Li Z., *The immersed interface method for elliptic equations with discontinuous coefficients and singular sources*, SIAM J.Num.Analysis 31, 4, 1019-1044 (1994)

[22] LeVeque R.J., *Numerical Methods for Conservations Laws,* Birkhäuser (1992)

[23] Malladi R., Sethian J.A., Vemuri B.C., *Shape Modeling with Front Propagation: A Level Set Approach*, IEEE Trans. on Pattern Analysis, 17, 2, 158-175 (1995)

[24] Mansury Y., Deisboeck T.S., *Simulating 'structure-function' patterns of malignant brain tumors*, Physica A, 331, 219-232 (2004)

[25] Morton K.W., Mayers D.F., *Numerical solution of partial differential equations*, Cambridge University Press (1994)

[26] Osher S., Fedkiw R., *Level Set Methods and Dynamic Implicit Surfaces,* Springer-Verlag, New York (2002)

[27] Osher S., Sethian J.A., *Fronts Propagating with Curvature-Dependent Speed: Algorithms Based on Hamilton-Jacobi Formulations*, J.Comp.Phys. 79, 12-49 (1988)

[28] Pao C.V., *Nonlinear parabolic and elliptic equations*, Plenum Press (1992)

[29] Preziosi L. (editor), *Cancer modeling and simulation*, Chapman&Hall (2003)

[30] Richtmyer R.D., Morton, K.W., *Difference methods for initial value problems*, Interscience Publishers (1967)

[31] Sethian J.A., *Level Set Methods and Fast Marching Methods,* Cambridge University Press (1999)

[32] Sethian J.A., *Curvature and the Evolution of Fronts,* Comm. in Math.Phys., 101, 487-499 (1985)

[33] Sethian J.A., *Numerical Methods for Propagating Fronts,* in Variational Methods for Free Surface Interfaces, Editors, P. Concus and R. Finn, Springer-Verlag (1987)

[34] Sethian J.A., *A Fast Marching Level Set Method for Monotonically Advancing Fronts*, Proceedings of the National Academy of Sciences, 93, 4 (1996)

[35] Sethian J.A., *Evolution, Implementation, and Application of Level Set and Fast Marching Methods for Advancing Fronts*, J. Comp. Phys. 169, 503-555 (2001)

[36] Shyy W., Udaykumar H.S., Madhukar M.R., Smith R.W., *Computational fluid dynamics with moving boundaries*, Taylor&Francis (1996)

[37] Smith G.D., *Numerical solution of partial differential equations: finite difference methods*, Oxford University Press (1985)

[38] Yanenko N.N., *The method of fractional time steps*, Springer (1971)

[39] Thomas J.W., *Numerical partial differential equations – Finite difference methods*, Springer (1995)

[40] Zheng X., Wise S.M., Cristini V., *Nonlinear simulation of tumor necrosis, neo-vascularization and tissue invasion via an adaptive finite-element/level-set method*, Bull.Math.Biol., in press (2004)

Appendix A *Discretization of the model equations*

Each of the model governing equations (2.12) and (2.15) can be cast in the general compact conservative form:

$$\frac{\partial \mu}{\partial t} = \nabla \bullet (Q \nabla \mu) - W \nabla \bullet (\mu \nabla \nu) + \Gamma(\mu) - L(\mu)$$

For the reasons stated at the beginning of Section 4, the equivalent non-conservative formulation is employed for the implementation here:

$$\frac{\partial \mu}{\partial t} = Q \nabla^2 \mu + \nabla \mu \bullet \nabla Q - W \nabla \mu \bullet \nabla \nu - W \mu \nabla^2 \nu + \Gamma(\mu) - L(\mu) \qquad \text{(A.1)}$$

In the solution formulation, the current time is $t_{n+1} = (n+1)\Delta t$, and the corresponding level set function is $\varphi_{i,j}^{n+1} = \varphi(x(i), y(j), t_{n+1})$ at all Cartesian grid points (i, j). The current domain occupied by the tumor is $\Omega_{n+1} = \Omega(t_{n+1}) = \{(i, j) \mid \varphi_{i,j}^{n+1} < 0\}$, while the domain occupied by the tumor at the previous time step is $\Omega_n = \Omega(t_n) = \{(i, j) \mid \varphi_{i,j}^{n} < 0\}$; in the outer environment we have $\Omega_{n+1}^{out} = \Omega^{out}(t_{n+1}) = \{(i, j) \mid \varphi_{i,j}^{n+1} > 0\}$ and $\Omega_n^{out} = \Omega^{out}(t_n) = \{(i, j) \mid \varphi_{i,j}^{n} > 0\}$. As a result of the Eulerian nature of the solution methodology, coupled with the inherent discontinuities across the tumor boundary, it is necessary to identify and treat separately two types of grid points:

1. $\{(i, j) \mid \varphi_{i,j}^{n} \varphi_{i,j}^{n+1} > 0\}$ - referred to as “well-behaved” grid points - namely, grid points that remain on the same side of the tumor boundary during the time increment from t_n to t_{n+1}. At “well-behaved” grid points, the mass balance equation (A.1) is valid

and the discrete solution $\mu_{i,j}^{n+1} = \mu(x(i), y(j), t_{n+1})$ at the current time step is obtained by using a forward Euler time integration:

$$\frac{\mu_{i,j}^{n+1} - \mu_{i,j}^{n}}{\Delta t} = Q_{i,j}^{n} \nabla^2 \mu_{i,j}^{n} + \nabla \mu_{i,j}^{n} \bullet \nabla Q_{i,j}^{n} - W \nabla \mu_{i,j}^{n} \bullet \nabla \nu_{i,j}^{n} - W \mu_{i,j}^{n} \nabla^2 \nu_{i,j}^{n} + \Gamma_{i,j}^{n} - L_{i,j}^{n} \tag{A.2}$$

2. $\{(i, j) \mid \varphi_{i,j}^{n} \varphi_{i,j}^{n+1} \leq 0\}$ - referred to "ill-behaved" grid points - namely grid points where the tumor boundary crosses over during the time step from t_n to t_{n+1}. At such "ill-behaved" points, a discontinuous change occurs during the time step and the mass balance equation (A.1) can no longer be employed; instead, the solution $\mu_{i,j}^{n+1} = \mu(x(i), y(j), t_{n+1})$ at the current time step is obtained by interpolation. If the tumor boundary falls directly on a grid point at the previous time step, then it is also classified as "ill-behaved."

In implementing this solution approach, it is assumed that the tumor boundary does not advance more than one mesh spacing in a time step – which is in fact required by the CFL stability condition (5.10) for the level set equation (5.7). As defined in Section 5, a "regular" grid point (either inside the domain occupied by the tumor or outside) is a point on the fixed Cartesian grid that has no neighbors on the tumor boundary (in either the horizontal (x) direction or the vertical (y) direction) while an "irregular" grid point (on each side of the tumor boundary) corresponds to a point on the fixed Cartesian grid that is adjacent to the boundary, either horizontally or vertically. We note that "ill-behaved" grid points can only be "irregular."

At "regular" and "well-behaved" grid points, the standard 5-points stencil is used to discretize the Laplace operator in (A.2):

$$\nabla^2 \mu_{i,j}^n \approx \frac{\mu_{i+1,j}^n - 2\mu_{i,j}^n + \mu_{i-1,j}^n}{h^2} + \frac{\mu_{i,j+1}^n - 2\mu_{i,j}^n + \mu_{i,j-1}^n}{h^2} \tag{A.3}$$

and similarly for $\nabla^2 \nu_{i,j}^n$. Centered differencing is used to approximate the first order spatial derivatives in each direction:

$$\begin{aligned} \nabla \mu_{i,j}^n \bullet \nabla \nu_{i,j}^n &= \frac{\partial \mu_{i,j}^n}{\partial x}\frac{\partial \nu_{i,j}^n}{\partial x} + \frac{\partial \mu_{i,j}^n}{\partial y}\frac{\partial \nu_{i,j}^n}{\partial y} \\ &\approx (\frac{\mu_{i+1,j}^n - \mu_{i-1,j}^n}{2h})(\frac{\nu_{i+1,j}^n - \nu_{i-1,j}^n}{2h}) + (\frac{\mu_{i,j+1}^n - \mu_{i,j-1}^n}{2h})(\frac{\nu_{i,j+1}^n - \nu_{i,j-1}^n}{2h}) \end{aligned} \tag{A.4}$$

and similarly for the term $\nabla \mu_{i,j}^n \bullet \nabla Q_{i,j}^n$.

In the case of an "irregular" horizontal grid point (i, j), where, for instance, $\varphi_{i,j}^n < 0$ and $\varphi_{i+1,j}^n > 0$, there is an interface point in the horizontal direction between $x(i)$ and $x(i+1)$ (label its location as x_b). By linear interpolation of the level set function, the value of x_b can be determined as follows:

$$x_b - x(i) = -(\frac{\varphi_{i,j}^n}{\varphi_{i+1,j}^n - \varphi_{i,j}^n})h \overset{not.}{=} \theta_x h \qquad (0 < \theta_x < 1) \tag{A.5}$$

If $|\theta_x h| \le \varepsilon << 1$, where ε is a small number (typically, ε is chosen relative to the grid size h), then the grid point (i, j) can be considered on the interface (we refer to this as the ε - test). More details on the actual choice of ε in the actual numerical simulations is given in the results Section 6. If the "irregular" grid point (i, j) is also "well-behaved" according to the criterion introduced above, then a second-order interpolating polynomial $p_{\mu}(x)$ in the x-direction is constructed using $h, \theta_x, \mu(x_b, y(j), t_n), \mu_{i,j}^n, \mu_{i-1,j}^n$ where $\mu(x_b, y(j), t_n)$ is computed from the corresponding prescribed boundary conditions applied at the boundary point $(x_b, y(j))$. Using this approach, the second derivative in (A.2) is approximated as

$$\frac{\partial^2 \mu_{i,j}^n}{\partial x^2} \approx p_{\mu}^{''}(x)\Big|_{x=x(i)} \qquad \text{(A.6)}$$

and the first derivative as

$$\frac{\partial \mu_{i,j}^n}{\partial x} \approx p_{\mu}^{'}(x)\Big|_{x=x(i)} \qquad \text{(A.7)}$$

The same procedure is used in the y-direction. Naturally, there will be "irregular" grid points that might have neighbors on the boundary both in the x- and y-direction. Similarly, individual second order interpolating polynomials are separately constructed for all the other model dependent variables involved in (A.2) and the corresponding spatial derivatives are approximated as in (A.6) and (A.7) above.

The general discussion on overall numerical stability presented in Section 4.3.1 holds here as well, with the constraint on the time step size dominated by the diffusion type terms (but now in two dimensions).

The model boundary conditions at every time step are handled here as follows: first, the continuity of the model dependent variables U_A, U_C and of their associated fluxes – here translating into the continuity of their normal derivatives - across the tumor boundary is employed to determine the actual values of U_A and U_C on the tumor boundary (the normal derivatives of U_A, U_C on each side of the tumor boundary are approximated by using one-sided differences in the normal direction). With the value of U_C known on the boundary, the prescribed Dirichlet boundary conditions (2.16) are employed to compute the values of U_T and U_N on the tumor boundary.

Once the discrete solution $\mu_{i,j}^{n+1} = \mu(x(i), y(j), t_{n+1})$ at the current time step has been computed at all the "well-behaved" grid points (i, j) - both "regular" and "irregular" – then the boundary values are updated as described above and finally, the solution $\mu_{i,j}^{n+1}$ at the remaining "ill-behaved" grid points at the current time step is obtained by interpolation. The boundary value is employed if the grid point is close enough to a boundary point (according to the ε - test) otherwise bilinear interpolation is used. This is the most straightforward approach; higher order interpolation formulas can also be employed.

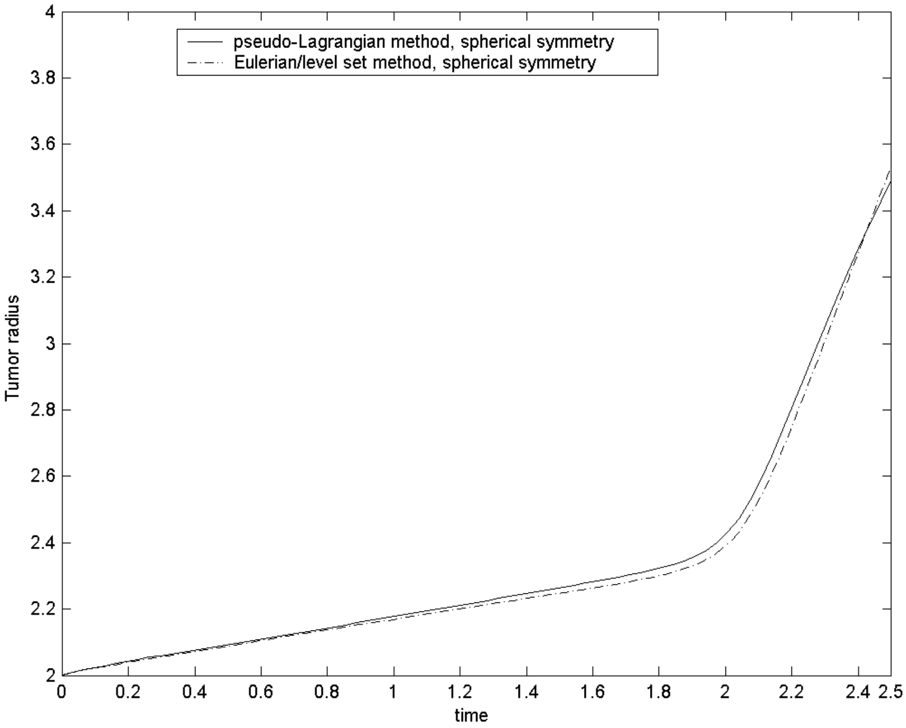

Figure 1: Comparison of the tumor radius evolution in time for the spherically symmetric geometry obtained using two solution methods: a pseudo-Lagrangian method and an Eulerian/level set method. The model parameters are given by (4.16) with initial tumor radius $R_0 = 2$ and outer environment radius $R_D = 10$.

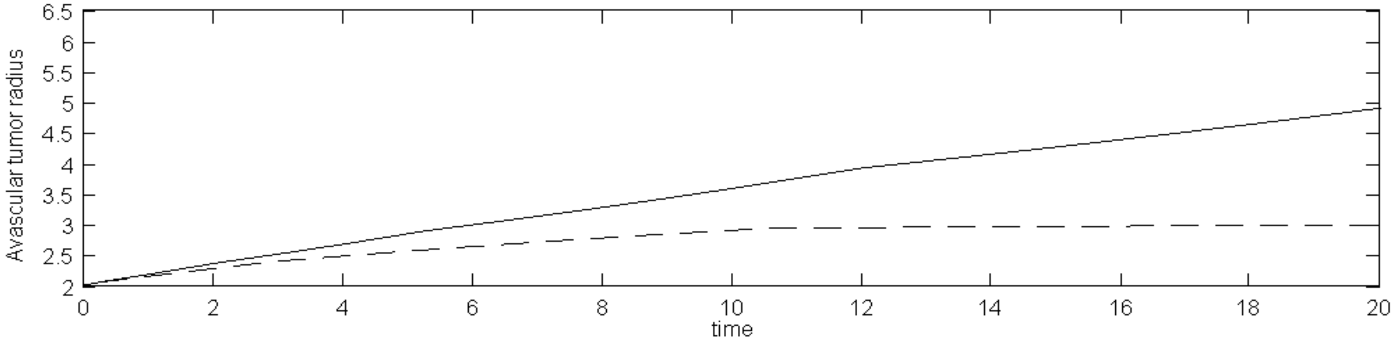

Figure 2: Evolution of the tumor radius in the absence of angiogenesis. The solid line corresponds to $\Delta_D = 0.001$ and the dashed line to $\Delta_D = 1$. The remaining model parameters are the same as Figure 1. A stabilized state is approached for $\Delta_D = 1$.

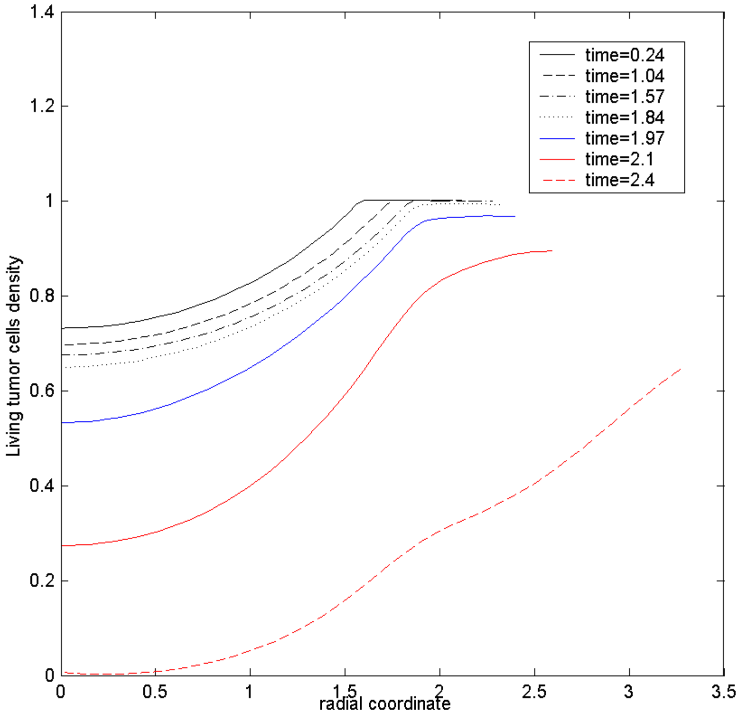

Figure 3: Evolution of the tumor living cell density at various moments in time for spherically symmetric tumor growth (Figure 1 parameters). The first four curves correspond to the avascular phase of tumor growth, the fifth one to an intermediate (vascularization) phase and the last two to a fully vascular phase.

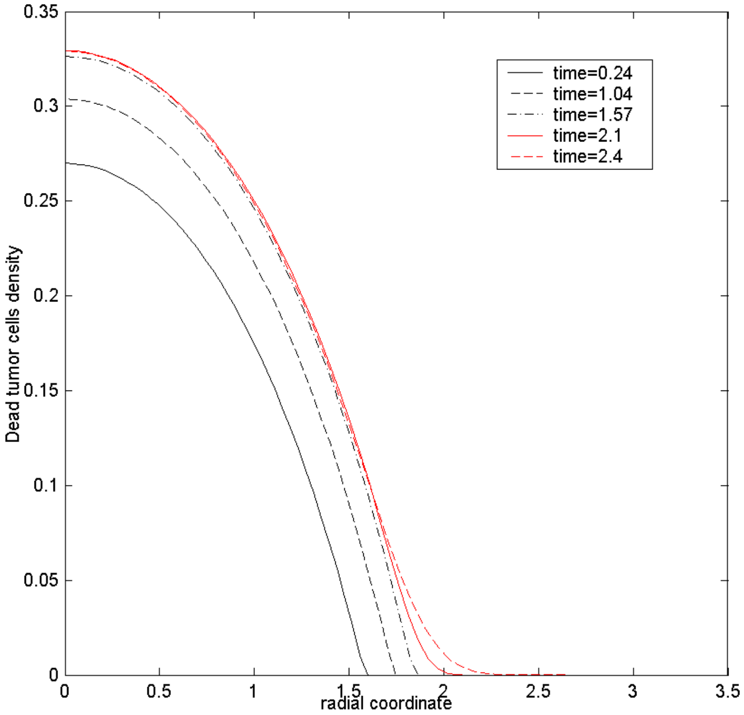

Figure 4: Evolution of the tumor dead cell density at various moments in time for spherically symmetric tumor growth (Figure 1 parameters). Formation of a necrotic core in the central region of the tumor observed.

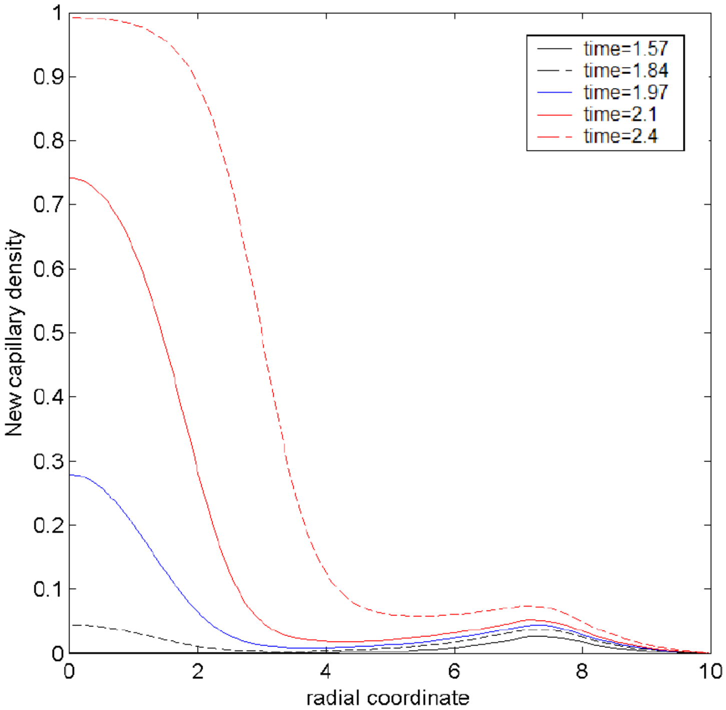

Figure 5: Evolution of the new capillary density at various moments in time for spherically symmetric tumor growth (Figure 1 parameters). The endothelial cells stimulated to proliferate belong to the pre-existing capillary network, here located on the line segment $7 \leq r \leq 8$..

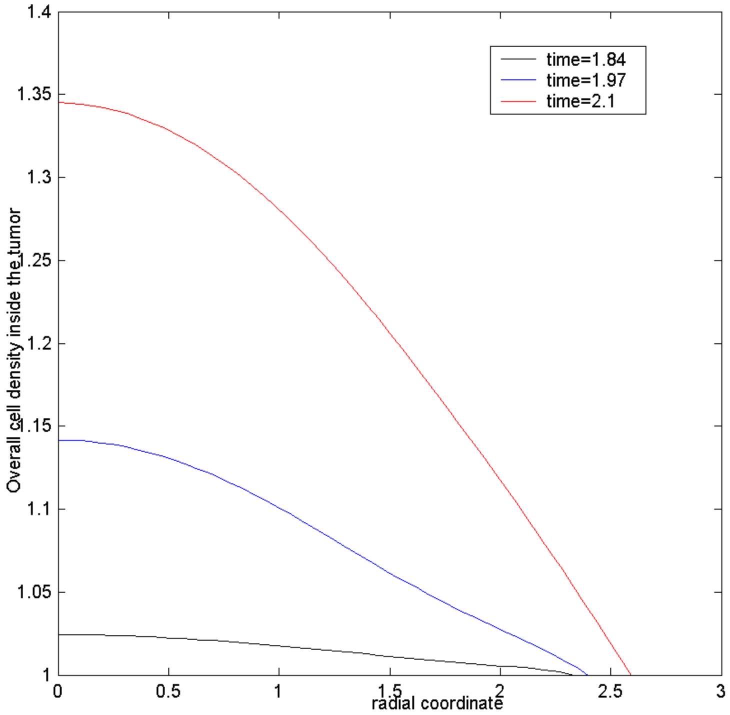

Figure 6: Evolution of the overall cell density inside the tumor at three moments in time for spherically symmetric tumor growth (Figure 1 parameters). Development of increasingly sharp local gradients occurs.

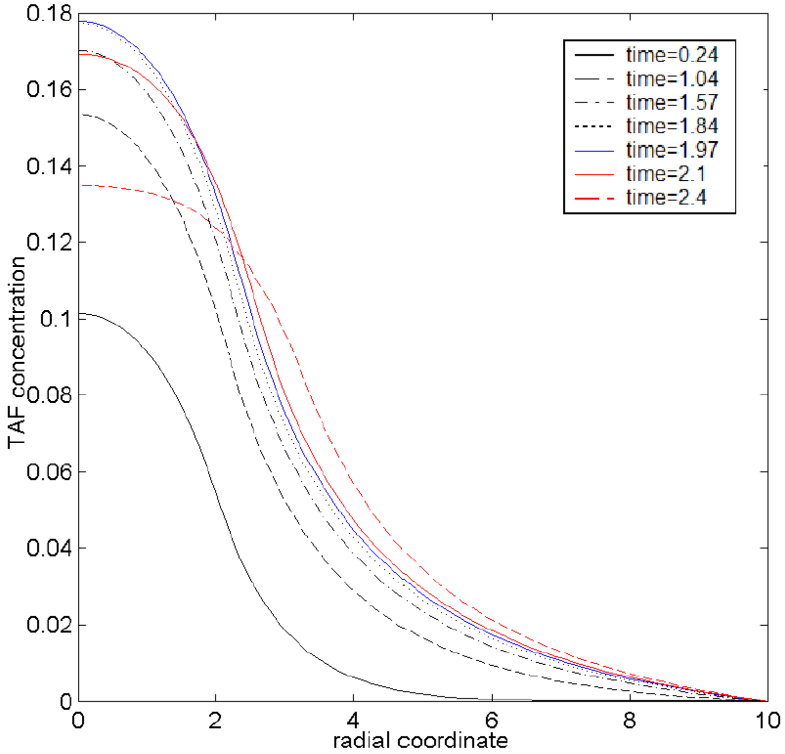

Figure 7: Evolution of the tumor angiogenic factor (TAF) at various moments in time, in the avascular and in the vascular phase of growth, for spherically symmetric tumor growth (Figure 1 parameters).

(a) avascular phase

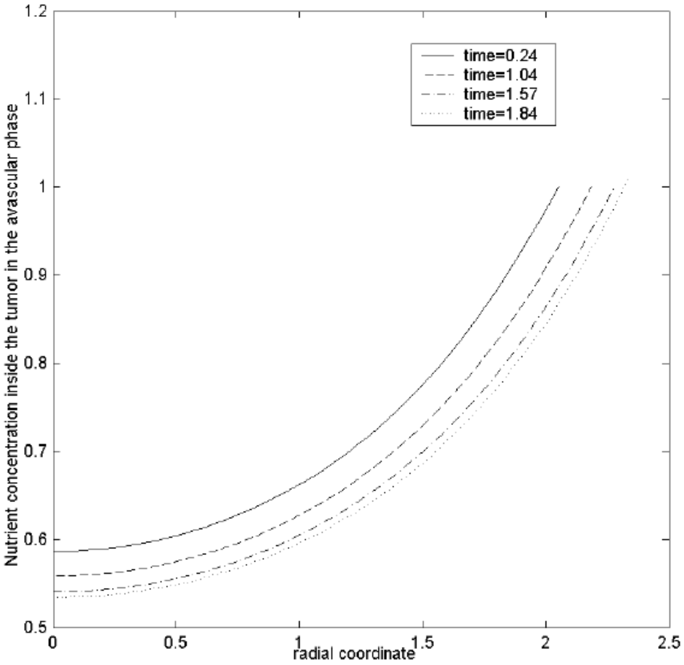

(b) vascular phase

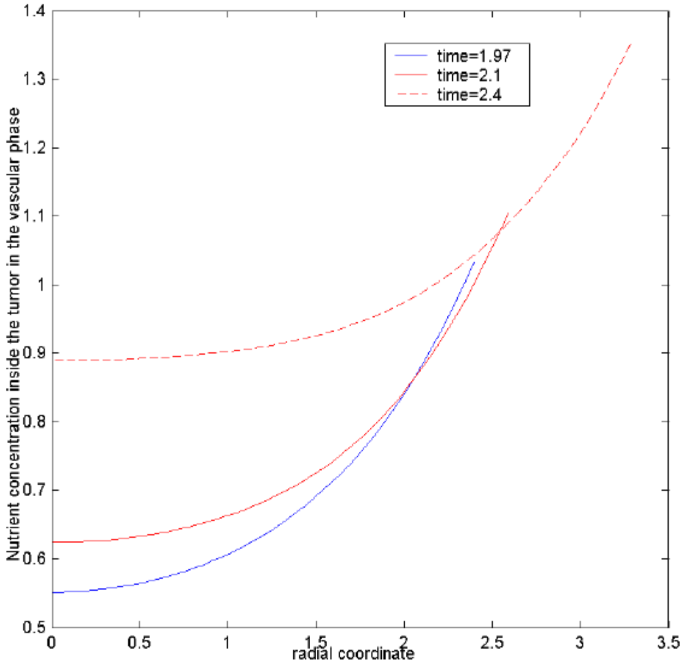

Figure 8: Nutrient evolution inside the tumor in the (a) avascular phase and in the (b) vascular phase of growth for spherically symmetric tumor growth (Figure 1 parameters). Nutrient levels are maximum at the tumor surface and gradually decreasing towards the center.

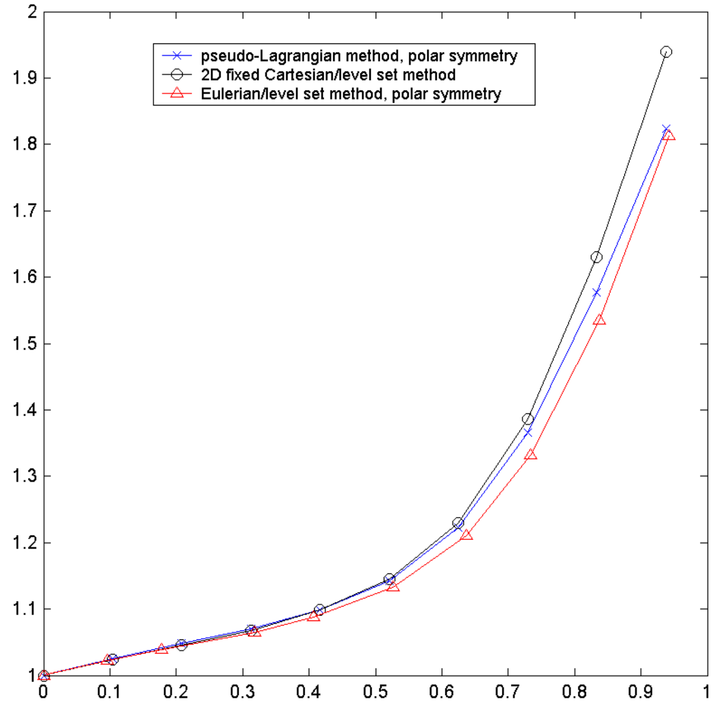

Figure 9: Comparison of the tumor radius evolution in time computed via three different methods: 2D Cartesian/narrow band level set method, 1D pseudo-Lagrangian method under the assumption of polar symmetry and a 1D Eulerian/level set method under the assumption of polar symmetry. The initial tumor boundary is a circle of center 0 and radius 1. The model parameters are given by (4.16), except that $\hat{U}_C = 0.5$ in the pre-existing capillary region.

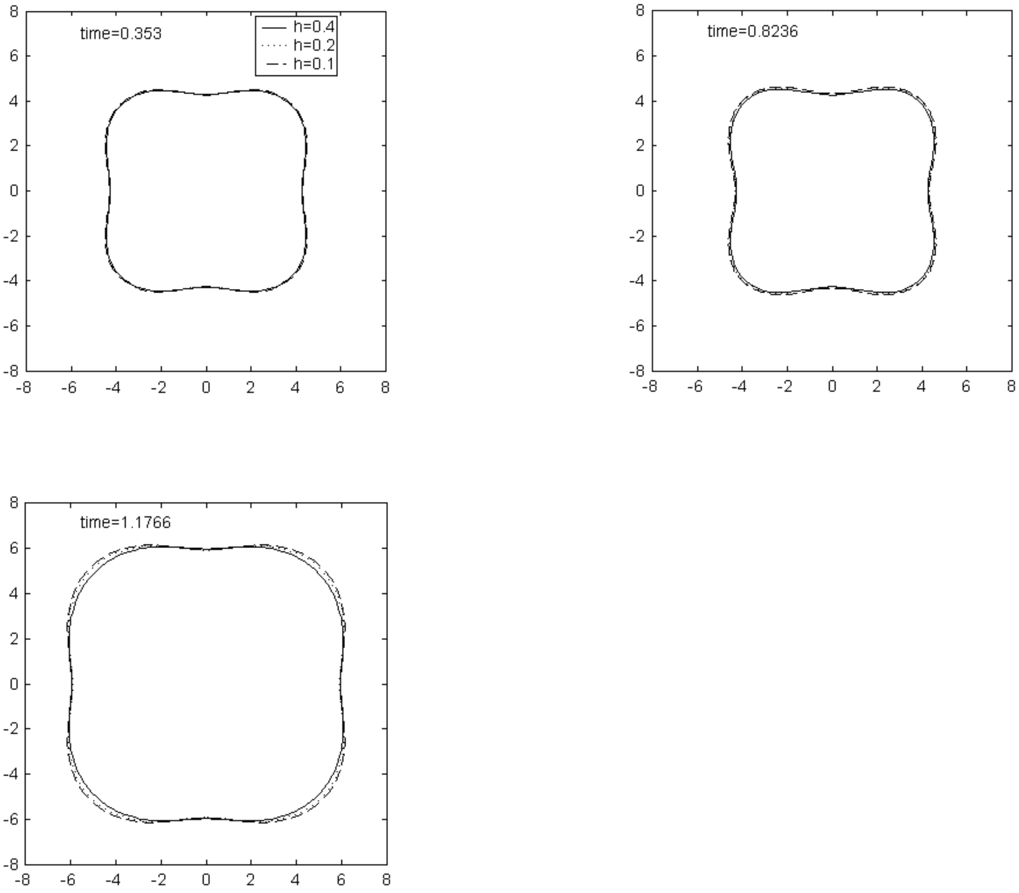

Figure 10: Mesh refinement analysis for the 2D simulations. The tumor initial boundary is defined by Eq. (6.1). Quantitative results are presented in Table 1.

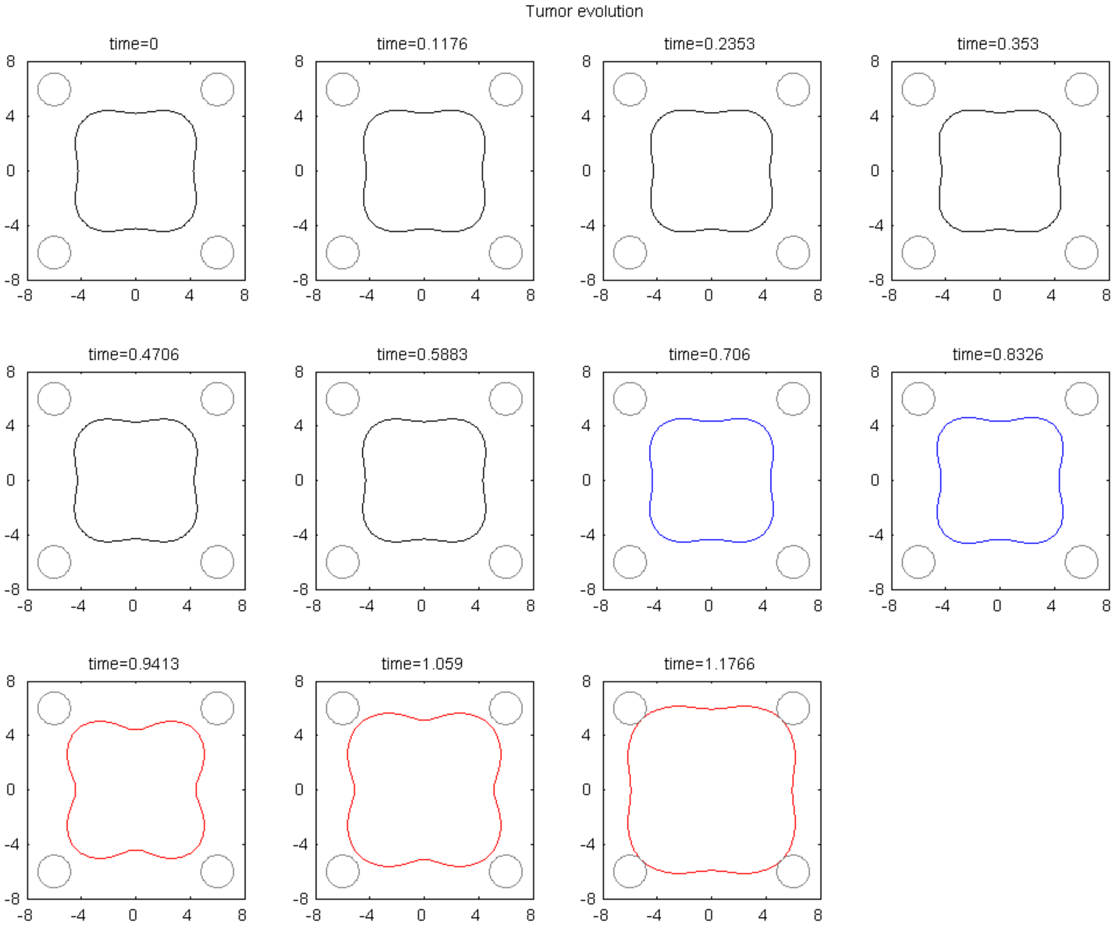

Figure 11(a): Evolution of the tumor in time, for the initial tumor boundary given by Eq.(6.1). The four small circles outside of the initial tumor boundary correspond to the location of the pre-existing capillaries. The model parameters are the same as Figure 9.

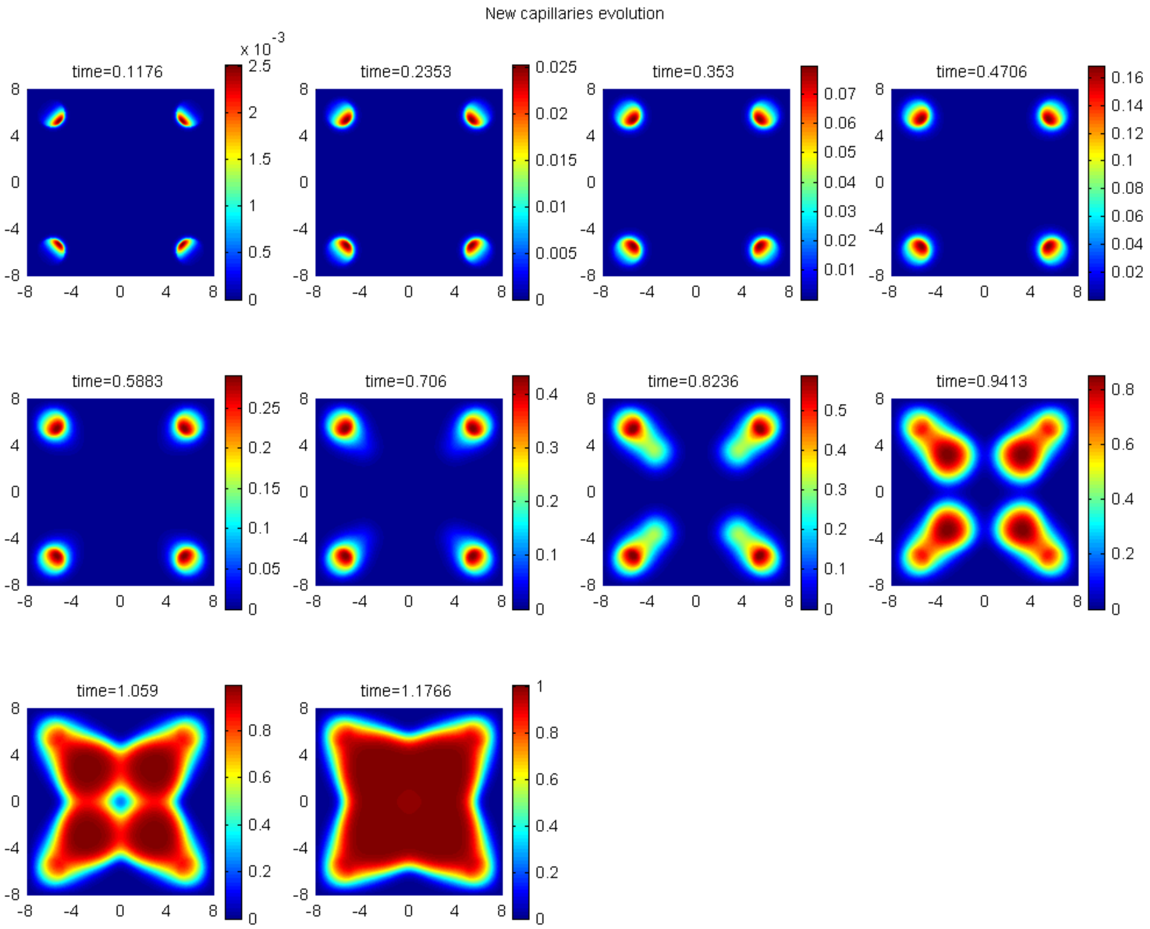

Figure 11(b-1): Evolution of the new capillary density displayed as contour plots for the conditions of Figure 11(a).

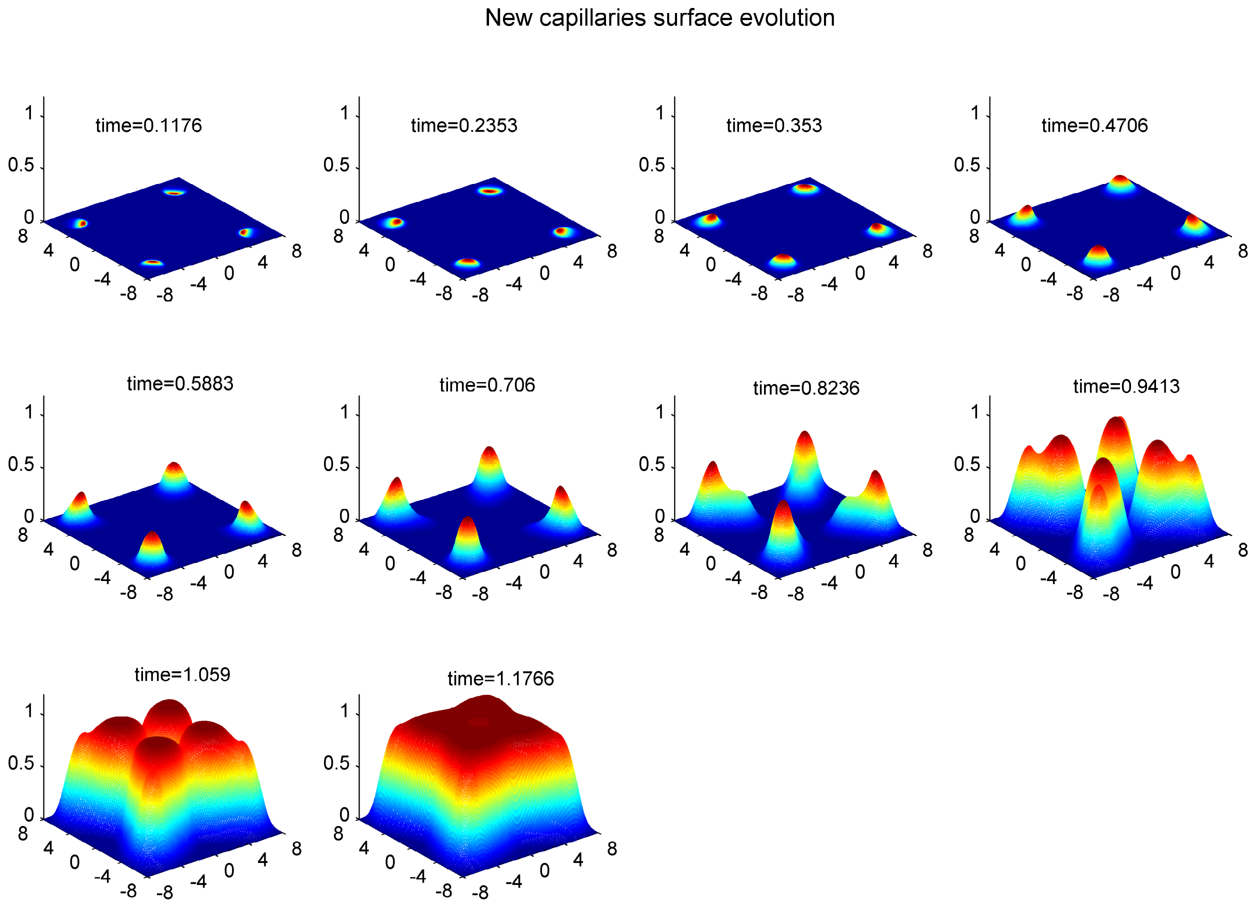

Figure 11(b-2): Evolution of the new capillary density displayed as surface plots for the conditions of Figure 11(a).

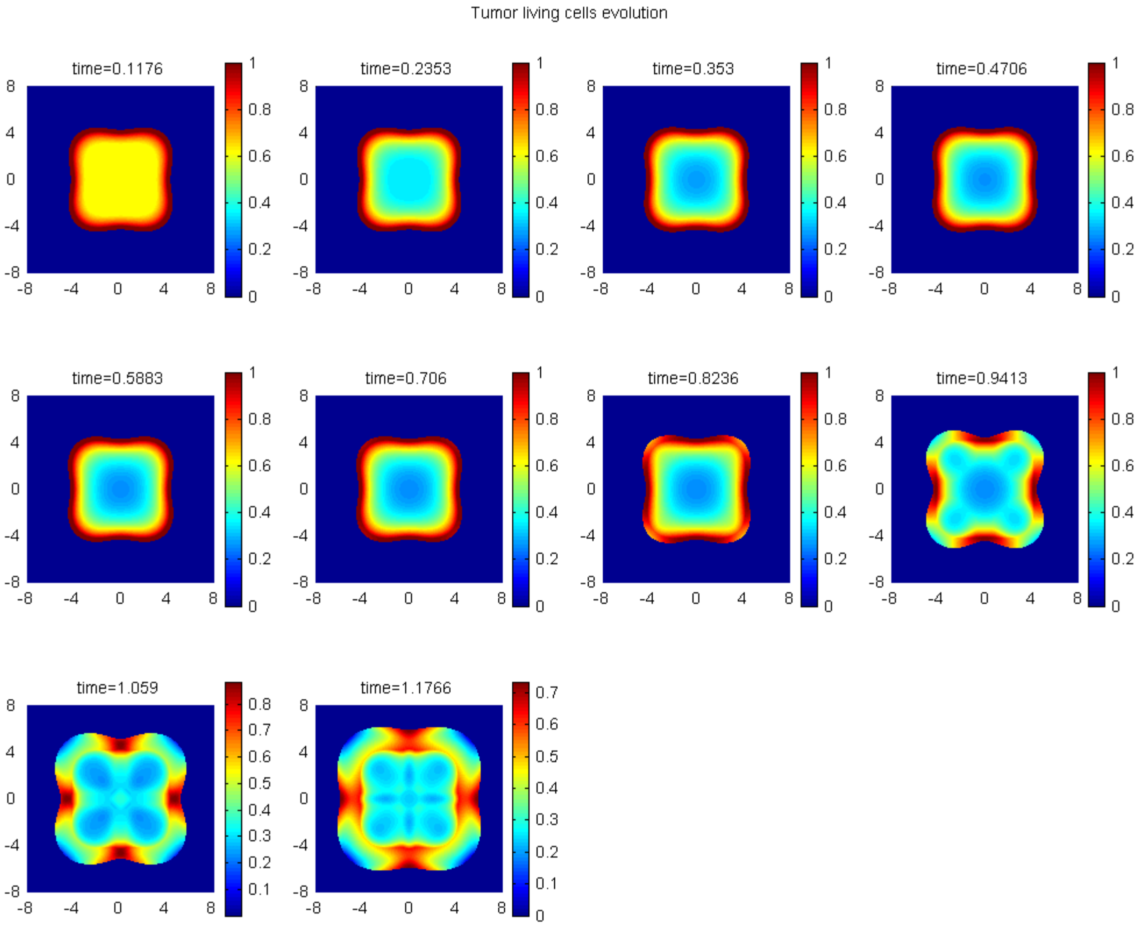

Figure 11(c): Evolution of tumor living cell density displayed as contour plots for the conditions of Figure 11(a).

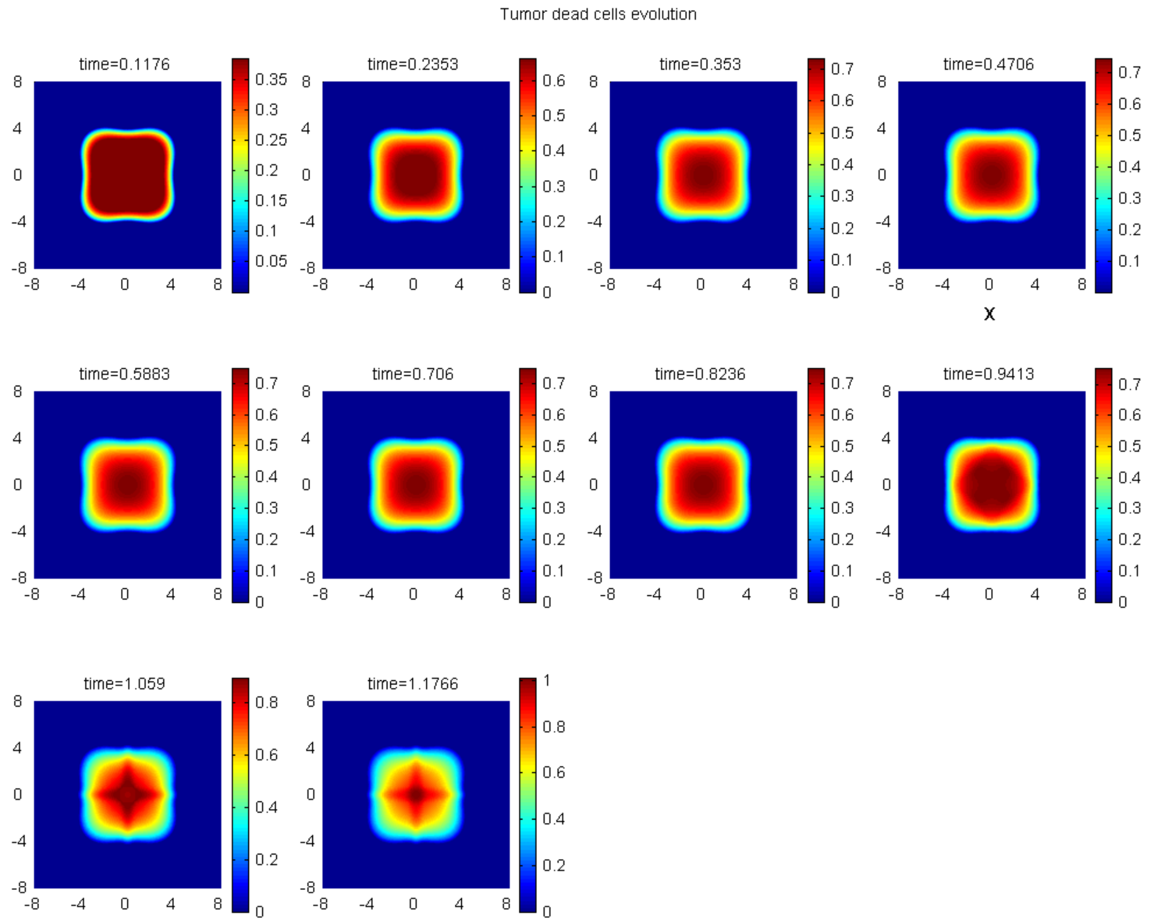

Figure 11(d): Evolution of tumor dead cell density displayed as contour plots for the conditions of Figure 11(a). The tendency to form a large necrotic region is observed.

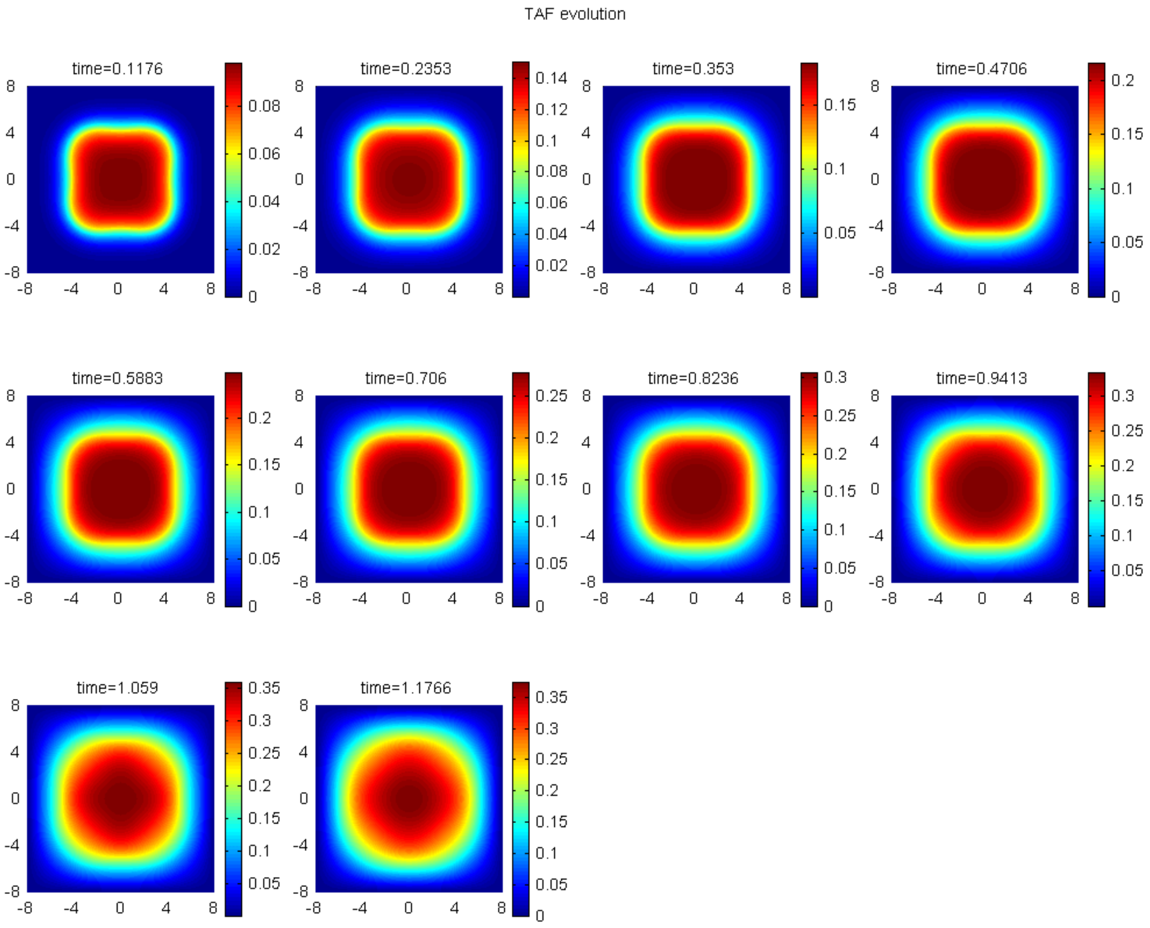

TAF evolution

time=0.1176 time=0.2353 time=0.353 time=0.4706

time=0.5883 time=0.706 time=0.8236 time=0.9413

time=1.059 time=1.1766

Figure 11(e): Evolution of tumor angiogenic factor (TAF) displayed as contour plots for the conditions of Figure 11(a).

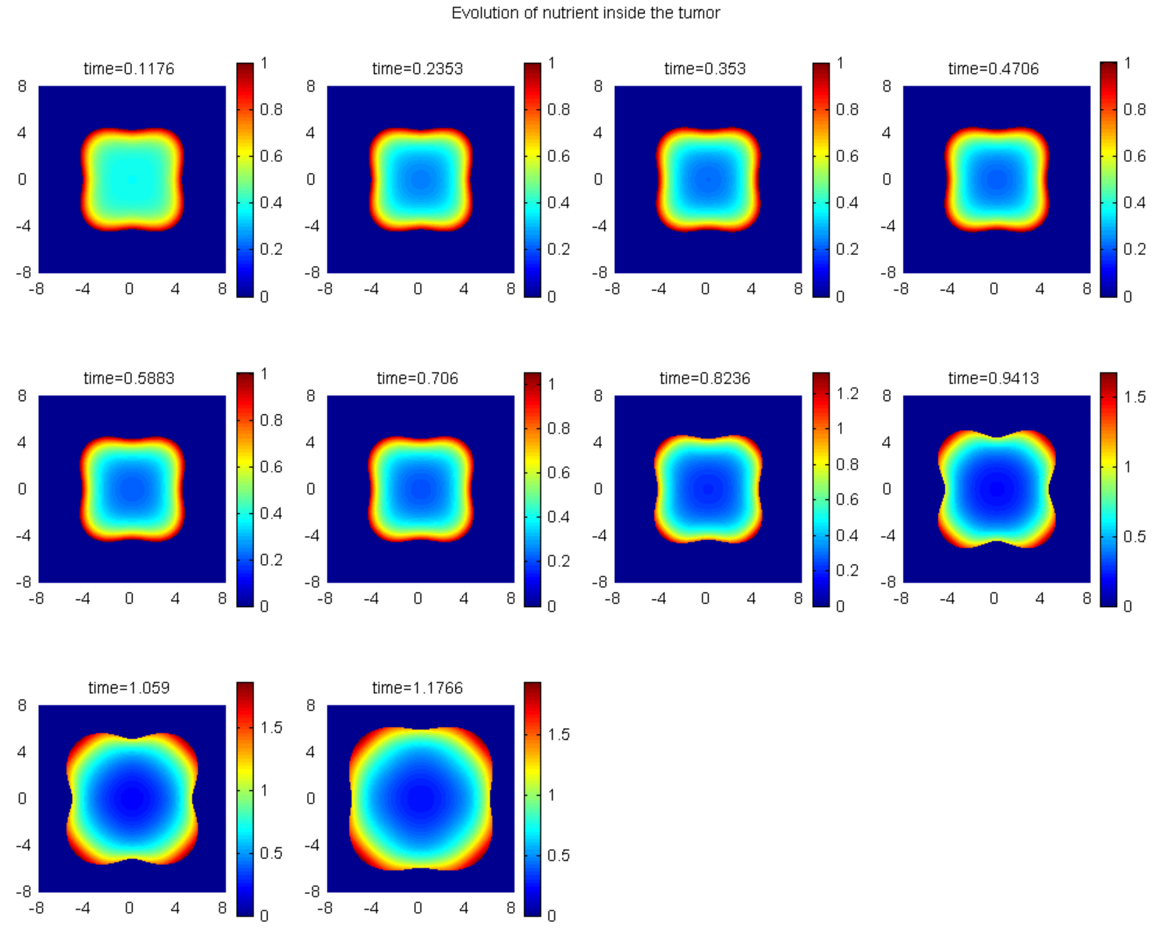

Figure 11(f): Evolution of nutrient concentration displayed as contour plots for the conditions of Figure 11(a).

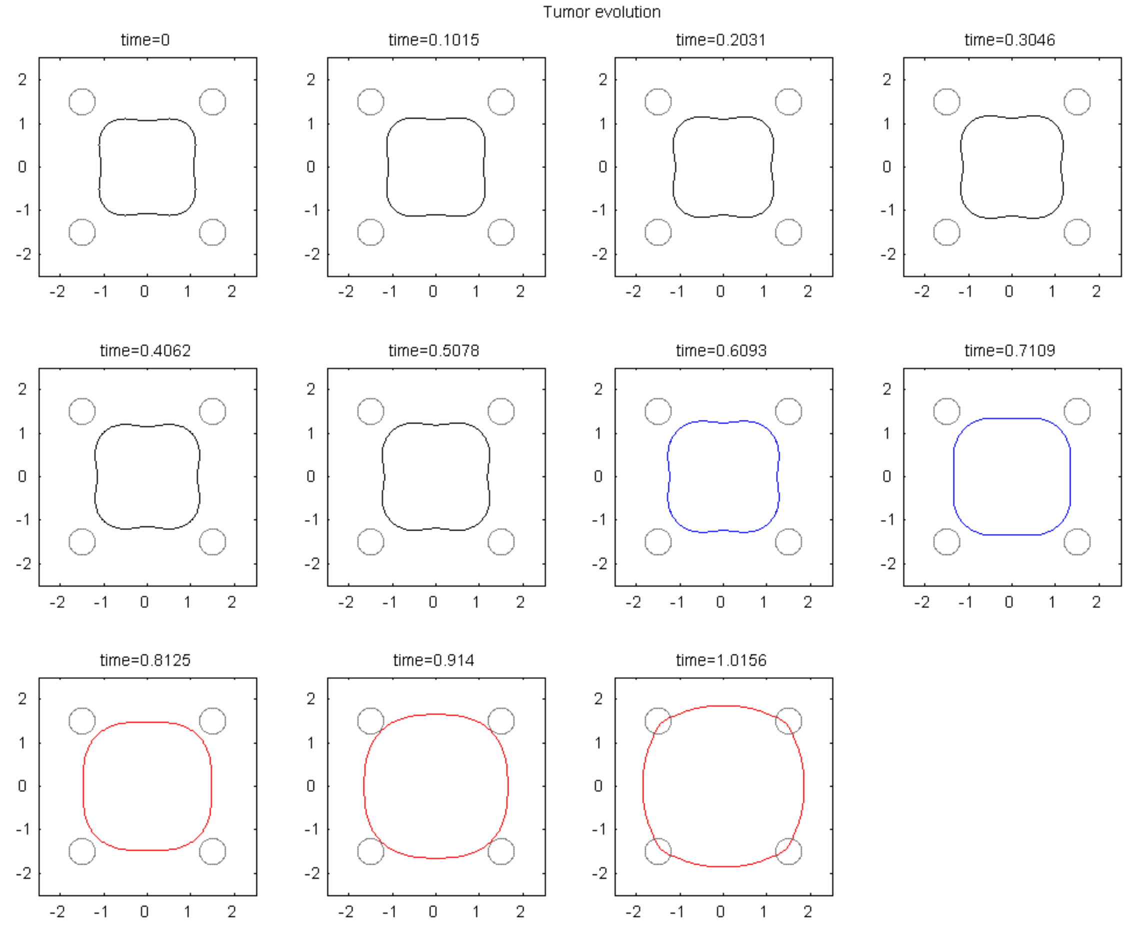

Figure 12(a): Evolution of the tumor in time, for the initial tumor boundary given by Eq.(6.4). The initial size of the tumor and the overall domain have been scaled down by a factor of four. The four small circles outside of the initial tumor boundary correspond to the location of the pre-existing capillaries. The model parameters are given by (4.16).

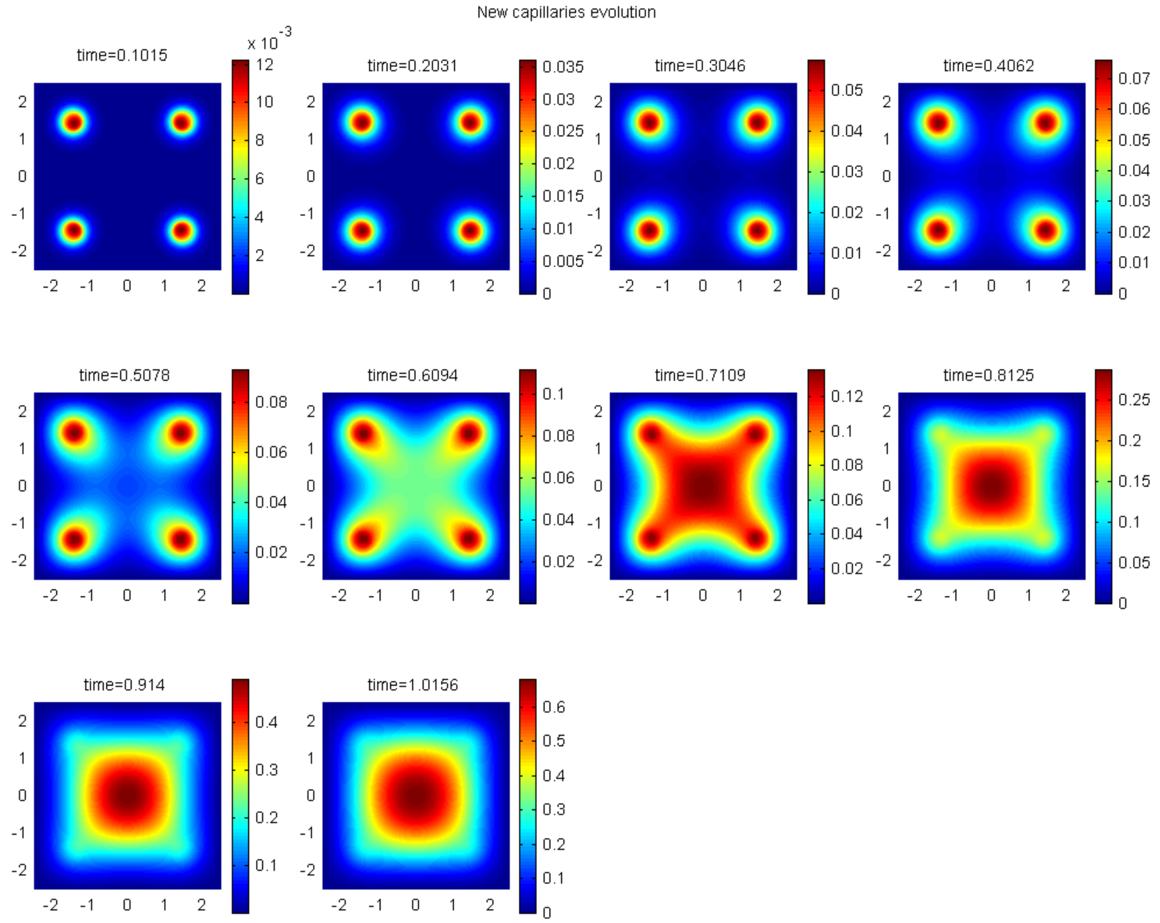

Figure 12(b-1): Evolution of the new capillary density displayed as contour plots for the conditions of Figure 12(a).

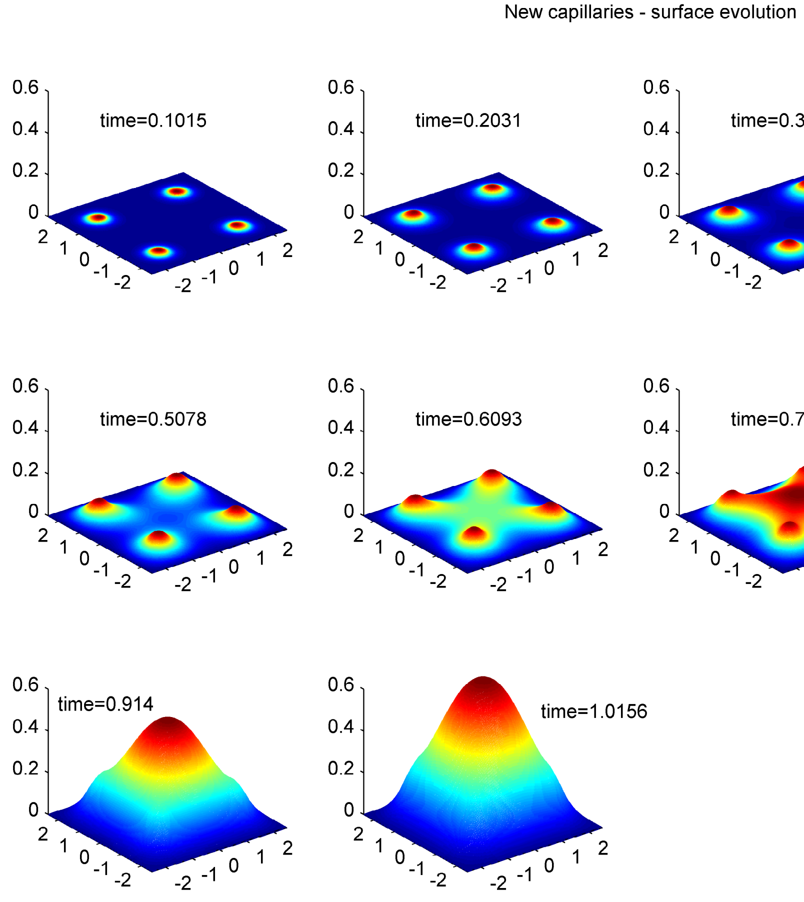

Figure 12(b-2): Evolution of the new capillary density displayed as surface plots for the conditions of Figure 12(a).

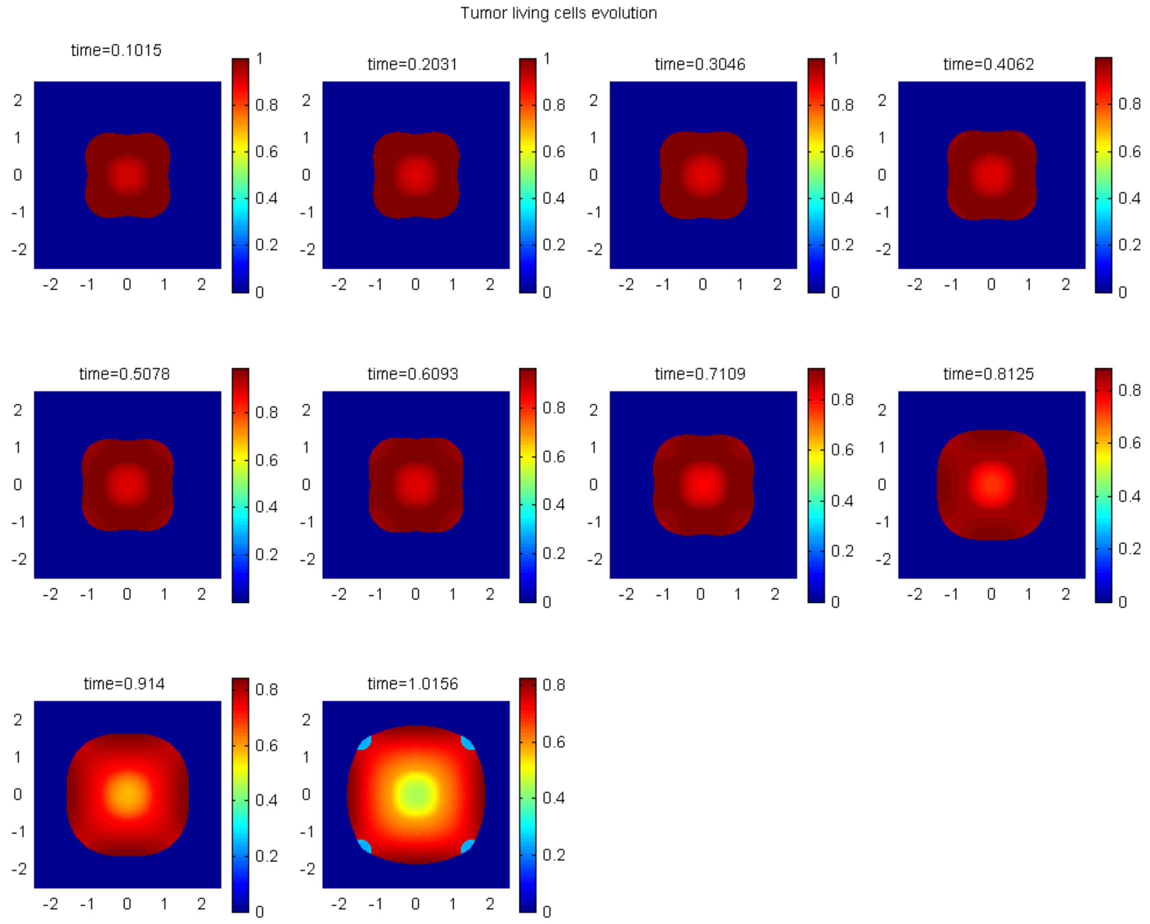

Figure 12(c): Evolution of tumor living cell density displayed as contour plots for the conditions of Figure 12(a).

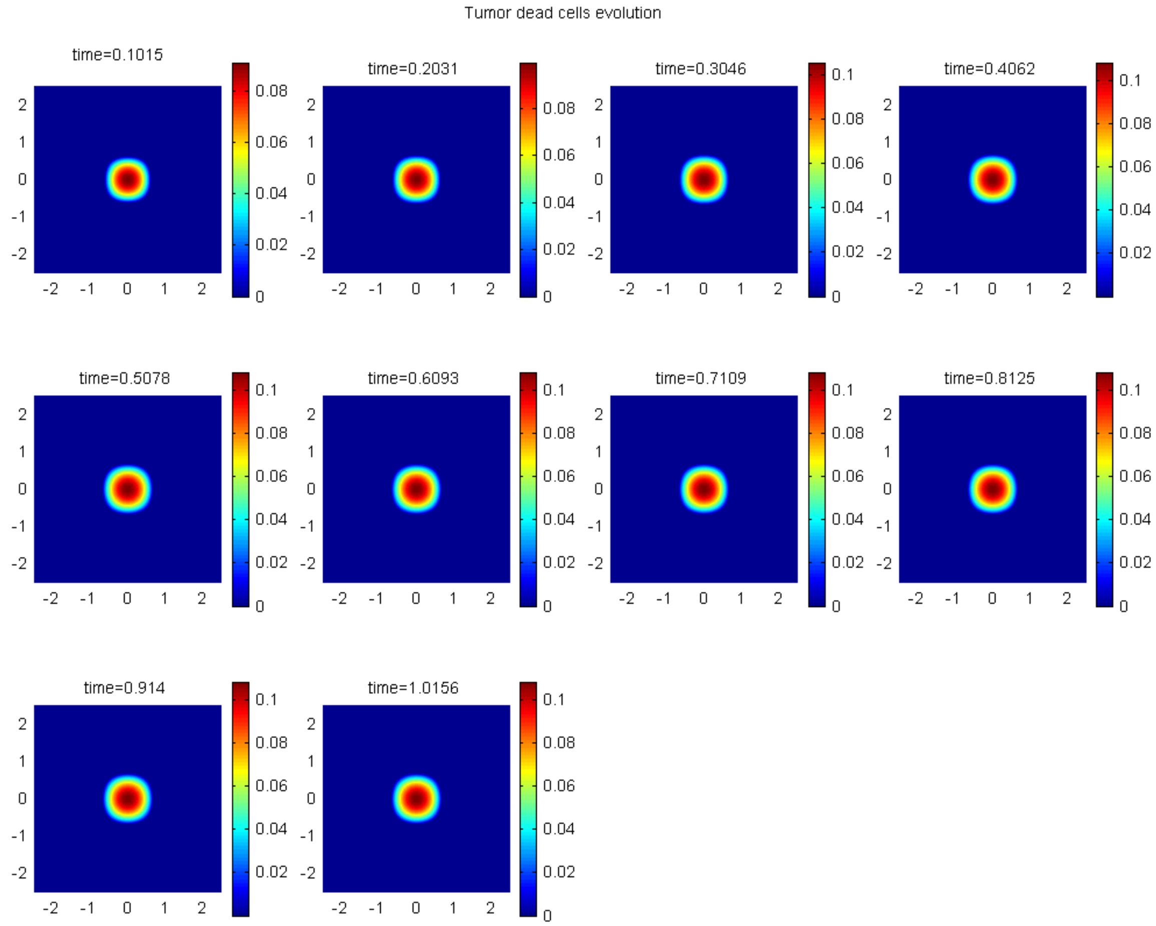

Figure 12(d): Evolution of tumor dead cell density displayed as contour plots for the conditions of Figure 12(a). The tendency to form a large necrotic region is observed.

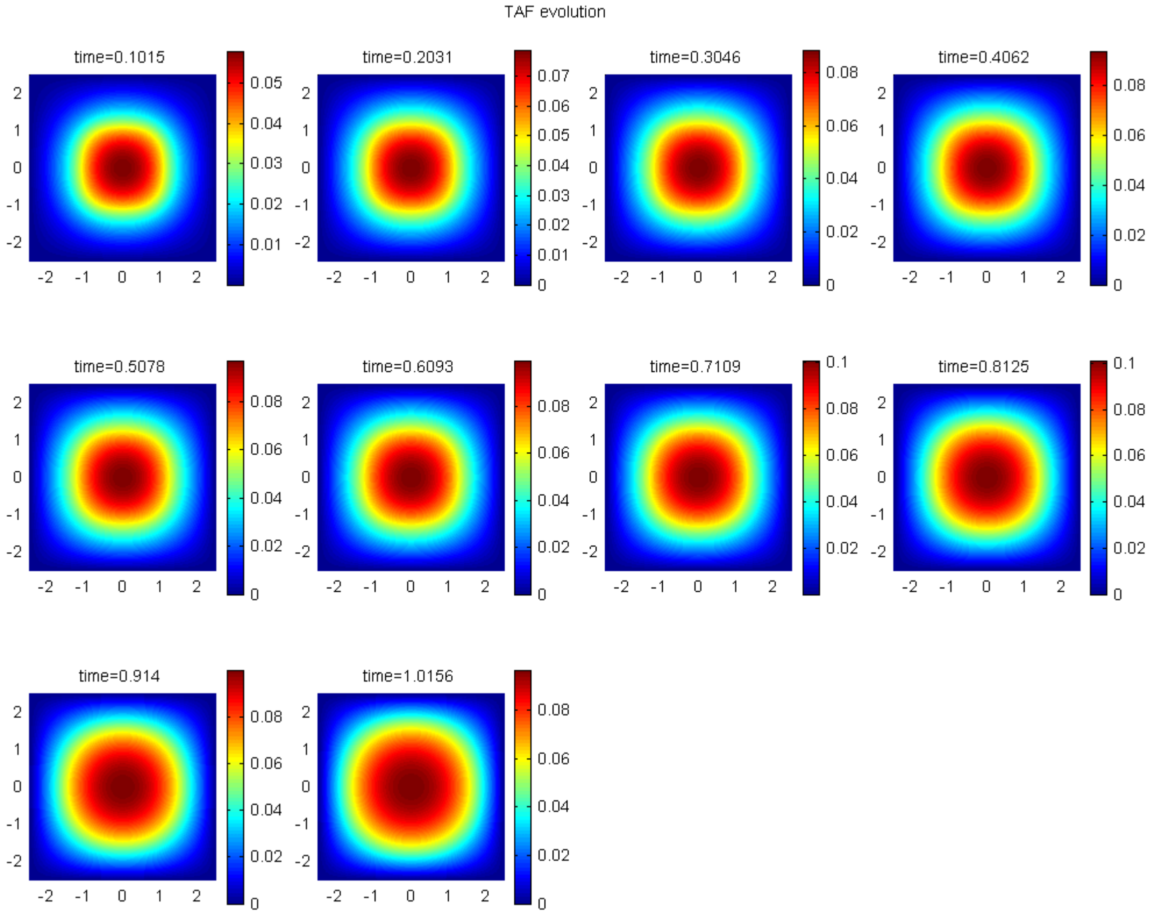

Figure 12(e): Evolution of tumor angiogenic factor (TAF) displayed as contour plots for the conditions of Figure 12(a).

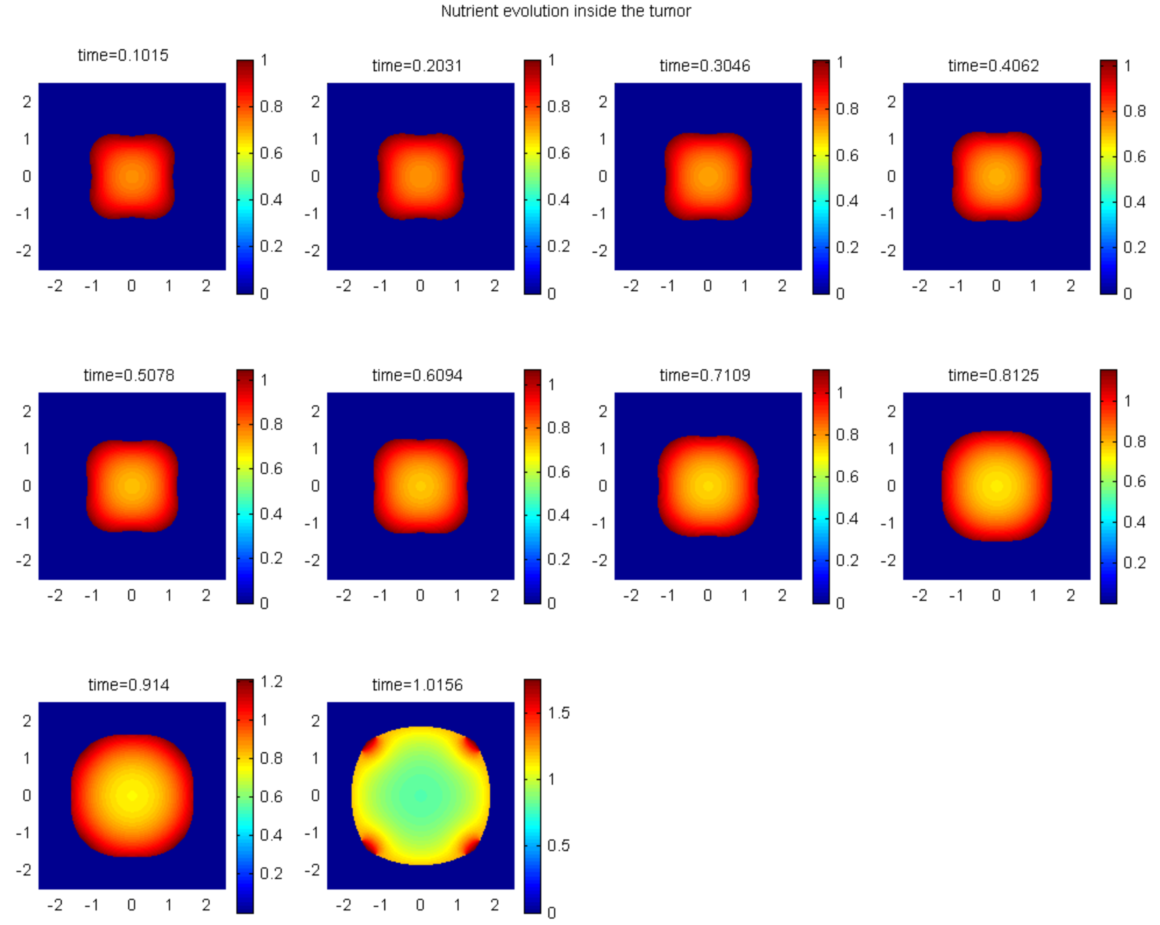

Figure 12(f): Evolution of nutrient concentration displayed as contour plots for the conditions of Figure 12(a).

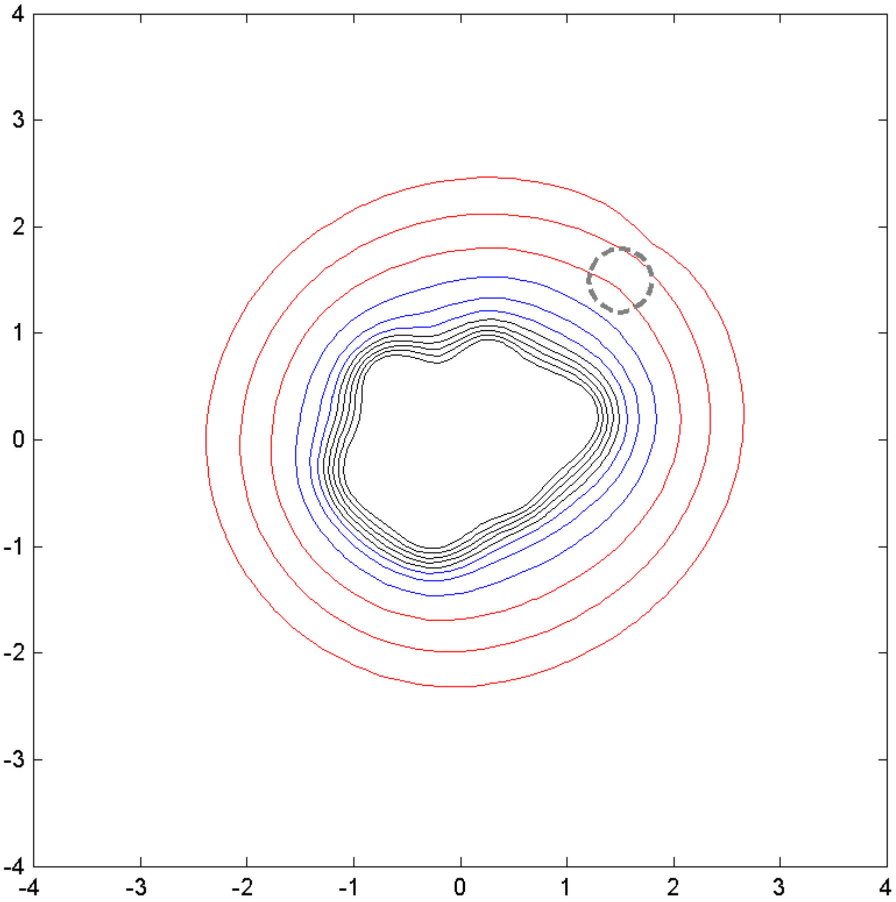

Figure 13: Evolution of an asymmetric, multimodal tumor boundary defined by Eq.(6.5) initially. The location of the existing capillaries is marked by the small dashed gray circle (centered at (1.5,1.5) with radius 0.3). Equal time increments of 0.25 are shown, from $t = 0$ to $t = 2.5$. Model parameters as in Figure 11, except that $\hat{U}_C = 0.5$ in the pre-existing capillary region, $\bar{U}_C = 0.4$ and $K_S = 10$.

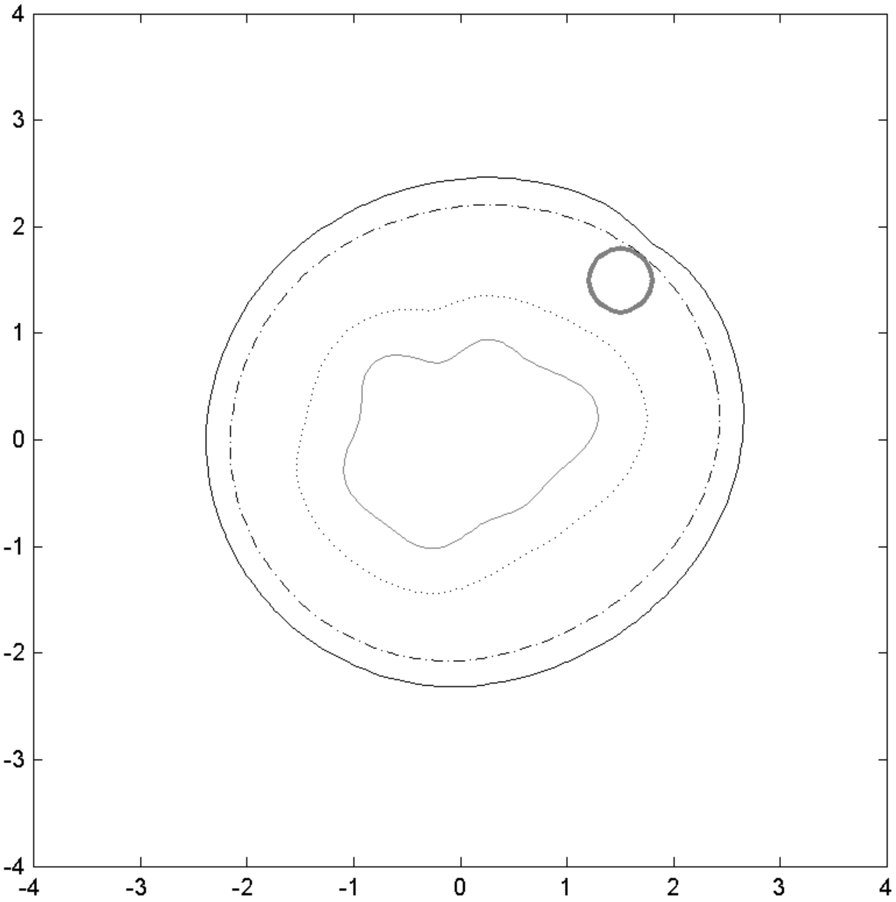

Figure 14: A comparison of the tumor boundary evolution for two model parameters characterizing the vascular phase of growth: K_S and Γ_C. The initial tumor boundary (same as Figure 13) is shown as the gray solid line. The tumor boundary at the final time $t = 2.5$ is shown as follows: $K_S = 10$ and $\Gamma_C = 10$, dotted line; $K_S = 0$ and $\Gamma_C = 100$, dash-dot line; $K_S = 10$ and $\Gamma_C = 100$, solid line.